

# Autoignition measurements and a validated kinetic model for the biodiesel surrogate, methyl butanoate

S. Dooley, H.J. Curran<sup>\*</sup>, J.M. Simmie

*Combustion Chemistry Centre, National University of Ireland, Galway, Ireland*

Received 16 October 2007; received in revised form 10 December 2007; accepted 23 January 2008

## Abstract

The autoignition of methyl butanoate has been studied at 1 and 4 atm in a shock tube over the temperature range 1250–1760 K at equivalence ratios of 1.5, 1.0, 0.5, and 0.25 at fuel concentrations of 1.0 and 1.5%. These measurements are complemented by autoignition data from a rapid compression machine over the temperature range 640–949 K at compressed gas pressures of 10, 20, and 40 atm and at varying equivalence ratios of 1.0, 0.5, and 0.33 using fuel concentrations of 1.59 and 3.13%. The autoignition of methyl butanoate is observed to follow Arrhenius-like temperature dependence over all conditions studied. These data, together with speciation data reported in the literature in a flow reactor, a jet-stirred reactor, and an opposed-flow diffusion flame, were used to produce a detailed chemical kinetic model. It was found that the model correctly simulated the effect of change in equivalence ratio, fuel fraction, and pressure for shock tube ignition delays. The agreement with rapid compression machine ignition delays is less accurate, although the qualitative agreement is reasonable. The model reproduces most speciation data with good accuracy. In addition, the important reaction pathways over each regime have been elucidated by both sensitivity and flux analyses.

© 2008 The Combustion Institute. Published by Elsevier Inc. All rights reserved.

**Keywords:** Methyl butanoate; Methyl ester; Biofuel; Biodiesel; Oxidation; Shock tube; RCM; Combustion; Modeling; Autoignition

## 1. Introduction

With the current uncertainty over the world's crude oil supply in terms of security and depletion, the development of renewable and alternative energy sources is of global importance. The recent report from the Intergovernmental Panel on Climate Change has highlighted the contribution that the transport sec-

tor makes to the high levels of CO<sub>2</sub> present in the atmosphere and has recommended the global use of biofuels as a means to curtail CO<sub>2</sub> production [1].

Biodiesel is a renewable fuel source suitable for use within the current transport sector infrastructure, as it shares similar physical properties with conventional crude-oil-derived fossil fuels [2]. What is known as biodiesel is a mixture of alkyl esters produced by a process of transesterification of various plant oils, and because the carbon contained in biodiesel has been derived from CO<sub>2</sub> already present in the atmosphere, it can be said to be a carbon-neutral fuel.

<sup>\*</sup> Corresponding author.  
E-mail address: [henry.curran@nuigalway.ie](mailto:henry.curran@nuigalway.ie)  
(H.J. Curran).

The chemical structure of biofuels significantly differs from that of fossil fuels due to the incorporation of oxygen atoms into the alkyl chain; as such, the chemical details of their combustion are currently poorly understood relative to those for more traditional fuels. As typical biodiesel components consist of alkyl chains that are 16–20 carbon atoms in length [3], their study is difficult from an experimental point of view and their simulation is currently too complex an undertaking. A common approach used to circumvent this problem is to select a surrogate molecule that represents the chemical properties of the real fuel to be studied [4,5].

Interest in methyl butanoate (MB) as a biodiesel surrogate was sparked in 2000 with the publication of a detailed chemical kinetic model to describe its combustion by Fisher and co-workers [6]. At that time there were only relatively unsophisticated measurements of the rate of MB oxidation [7–10] available to validate their work.

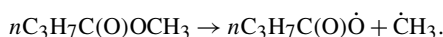
Since then MB has appeared more regularly in the literature: Marchese et al. [11] studied MB oxidation in a flow reactor at 12.5 atm using 800 ppm MB at equivalence ratios of 0.35, 1.0, and 1.5. Reactant, intermediate, and product species were quantified at a residence time of 1.8 s over the temperature range 500–900 K. The authors report that the kinetic model of Fisher et al. was in good agreement with experiment under stoichiometric conditions, but showed too high a reactivity when fuel-rich and too low a reactivity when fuel-lean.

These flow reactor data [11] were reported in 2007 by Gail et al. [12], who also presented measurements of MB oxidation in a jet-stirred reactor (JSR) and in an opposed-flow diffusion flame. MB and a host of intermediate species were quantified at a residence time of 70 ms in the JSR at an equivalence ratio of 1.13 over the temperature range 800–1275 K at 1 atm using 0.075% MB diluted in nitrogen. The opposed-flow diffusion flame measurements were performed for a stream of 4.7% MB diluted in N<sub>2</sub> at the bottom inlet and a stream of 42% O<sub>2</sub> also diluted in N<sub>2</sub> at the top inlet. MB and a host of intermediate species were again quantified. Simulations using a slightly modified version of the Fisher model well reproduced the flow reactor data at  $\phi = 0.35$  and  $\phi = 1.0$ ; however, reactivity at  $\phi = 1.5$  was greatly over-predicted. Agreement with JSR data was reasonable, although activity was underpredicted at low temperatures for MB and various intermediate species. The same model was not able to reproduce the opposed-flow diffusion flame data, showing, in general, higher reactivity for intermediate species and lower reactivity for MB than observed in experiment.

The same opposed-flow diffusion flame data were presented with additional JSR data by Sarathy et

al. [13], who performed a comparative experimental study of the oxidation of MB and a saturated methyl ester, methyl crotonate. The peak major intermediate species mole fractions were reported along with select species profiles, including MB at a residence time of 70 ms as a function of reactor temperature (850–1350 K) for a mixture of 0.075% MB  $\phi = 1.0$  at 1 atm.

Schwartz et al. [14] used a co-flowing methane/air nonpremixed flame doped with 5000 ppm MB and measured major species from within the flame using mass spectrometry. The authors were able to use their results to show that the rate of MB decomposition was consistent with a unimolecular decomposition reaction:



The only previously reported ignition delay times for MB in the gas phase have been by our own group in a comparative study on the oxidation of ethyl and methyl esters [15]. A mixture of 1% MB was studied under stoichiometric conditions in argon at 1 and 4 atm over the temperature range 1250–1666 K. We were able to modify the kinetic model of Fisher et al. to reproduce the ignition delay data, and this modified model served as a starting point for the further validated kinetic model presented in this study.

Vaughan et al. [16] also measured ignition delay times for MB, albeit in the liquid phase. A 1.1-s drop tower was used to study the autoignition of a series of methyl esters. Ignition delays were reported for MB droplets 0.9–1.5 mm in diameter at 1 atm for furnace temperatures of 1210–1253 K. Currently the convenient simulation of this type of combustion environment and that presented by the co-flow flame is not possible with a large kinetic model. Regrettably, the kinetic model presented in this study has not been tested against the data of Schwartz et al. or of Vaughan et al. at this time.

Elsewhere, El-Nahas et al. [17] performed a theoretical study at the CBS-QB3 level of theory into bond dissociation energies and the reaction pathways of MB decomposition. Their findings amount to a number of significant differences in comparison to the thermochemistry used by Fisher et al.

In another purely computational study, Westbrook et al. [18] used the unvalidated kinetic model of Fisher et al. to theorize that specifically MB, but by extension biodiesel, would be a less effective soot-reducing agent than other oxygenated hydrocarbons because of the C(O)–O–C linkage.

The aim of *this study* is to provide more information on the combustion characteristics of MB and to extend the range of the previously published detailed chemical kinetic mechanism of Metcalfe et al. [15] in

order to enhance our knowledge of the oxidation and soot reduction processes of biodiesel fuels.

## 2. Experimental

### 2.1. Shock tube

The fully characterized [19] shock tube facility has been described previously [20] and is validated on a regular basis against recent experiments on *n*-heptane oxidation from the Stanford group [21]. Briefly, our steel shock tube consists of a large but short (52-cm-diameter and 63-cm-long) driver section coupled via a 10-cm-long transition piece to the test section, which is 622 cm long and 10.24 cm in internal diameter. A polycarbonate diaphragm separates the high-pressure driver section from the low-pressure test section. Shock waves were generated by allowing the diaphragm to burst under pressure with the assistance of a cross-shaped cutting device that petaled the diaphragm. Pressure transducers (PCB Piezotronics, Model 113A21) were set into the final 50 cm of the test section and were used to measure the incident shock velocity with the aid of three universal time counters (Fluke PM6666). To allow for shock attenuation, the shock velocity at the end wall is calculated by extrapolating the incident velocities to the end wall. Reflected shock conditions were calculated using the usual one-dimensional shock relations [22] and the application GasEq [23], using initial temperatures in the range 290–300 K and initial pressures in the range 12–100 Torr.

In this study, test mixtures were prepared in a 50-L stainless steel tank using standard manometric methods. Gases were obtained from BOC Ireland Ltd.: helium CP Grade 99.999%, argon Zero Grade 99.998%, and oxygen Research Grade 99.985%. All gases were used without further purification. Methyl butanoate was obtained from Aldrich Chemical Co. Ltd. and was determined to be 99.75% pure by GC analysis. To minimize the presence of atmospheric air in the sample, the liquid fuel was dried with a molecular sieve overnight before being subjected to several freeze–pump–thaw degassing cycles before use. Liquid fuel was incorporated into the test mixture by vaporization into the evacuated ( $10^{-6}$  Torr) mixing tank. Partial pressures of fuel and oxygen were measured using a 100-Torr Baratron gauge to an accuracy of 0.01 Torr. Argon was added using a 900-Torr digital manometer (Chell cd101). Test gas mixtures were normally made up to a final pressure of 800 Torr and allowed to stand for at least 12 h to ensure homogeneity.

Light emission was observed using an end-on detection diagnostic that consisted of a PDA55 (switchable gain, amplified silicon detector) located behind

a 431.5-nm ( $\text{CH}^*$  emission) narrow-bandpass filter with a spectral bandwidth of 10 nm. The filter and the PDA were aligned behind a quartz window located in the end wall. A Kistler pressure transducer, mounted flush with the end wall, signaled the shock wave arrival at the end wall and the beginning of the ignition delay period. The end of the period was defined as the maximum rise in the rate of  $\text{CH}^*$  emission. Ignition delay times for each mixture studied were measured at reflected shock pressures of 1.0 ( $\pm 0.1$ ) atm and 4.0 ( $\pm 0.1$ ) atm.

The estimation of experimental error of shock tube ignition delays is difficult as the reflected shock conditions ( $T_5$  and  $P_5$ ) are calculations based on ideal shock wave theory. However, as  $T_1$  and  $P_1$  are accurately known,  $\pm 0.1$  K and  $\pm 0.01$  Torr, respectively, the measurement of the incident shock velocity is likely to be the largest source of error. To this end we have assumed a maximum error of  $\pm 0.3\%$  in the measurement of the time taken for the incident shock wave to travel from one pressure transducer to another. Any error in the extrapolation of the measured incident shock velocities to the shock velocity at the end wall would result in an average error of  $\approx \pm 7$  K in our calculation of the reflected shock temperature ( $T_5$ ).

The error in the determination of the ignition delay time is generally small as the rate of increase in  $\text{CH}^*$  emission is sudden and can easily be identified. We prefer to quantify uncertainty in ignition delay by determining the reproducibility of results. For example, the delay times at approximately 1540 K for the  $\phi = 1.0$  data set exemplify the level of reproducibility (the ignition delay times are within 9  $\mu\text{s}$  of one another) and go some way to quantifying this experimental error.

### 2.2. Rapid compression machine

The NUIG rapid compression machine (RCM) has a twin-opposed-piston configuration described previously [24,25], resulting in a fast compression time of approximately 16 ms. Two pistons of diameter 3.4 cm, driven by compressed air, move simultaneously to confine the test gas mixture into a compressed chamber volume of approximately 45  $\text{cm}^3$  without rebound. This compression results in a rapid increase in temperature and pressure, which is suitable for the study of autoignition under HCCI-like conditions. The compression ratio used for this study was approximately 10.9:1. Creved piston heads are used to improve the postcompression temperature distribution in the combustion chamber [26]. This particular design was adopted after computational fluid dynamic studies on the NUIG RCM [27] following similar work at MIT [28], which found that the creviced

Table 1  
Mixture composition for shock tube study

Mix	$\phi$	MB	O <sub>2</sub>	Ar
1	0.25	0.01	0.26	0.73
2	0.50	0.01	0.13	0.86
3	1.00	0.01	0.065	0.925
4	1.50	0.015	0.065	0.92

design resulted in an almost homogeneous temperature field in the postcompression period; that obtained with flat piston heads is far less homogeneous.

Test gas mixtures were prepared similarly to those in the shock tube study. However, the mixing tank was always flushed with the diluent it was to contain for the next test mixture before being evacuated to  $10^{-2}$  Torr. Partial pressures of fuel and all gases were measured using a 2000-mbar digital manometer (Chell cd101) to an accuracy of  $\pm 0.2$  mbar. Test gas mixtures were made up to a final pressure of 1800 mbar and were allowed to stand for at least 12 h to ensure homogeneity. The exact composition of mixtures used in this study are shown in Tables 1 and 2.

### 2.2.1. Temperature control

MB was mixed with oxygen and a nonreactive diluent gas (either argon and/or nitrogen), the proportions of diluent were varied to alter the overall heat capacity of each mixture, and hence the specific heat ratio,  $\gamma = C_p/C_v$ . Using nitrogen only as the diluent allows lower compressed gas temperatures,  $T_C$ , while pure argon reaches much higher temperatures following compression due to its lower heat capacity. Further control of the compressed temperature was achieved by using a well-insulated heating blanket, which surrounded the combustion chamber and piston sleeves. This facility allowed the initial temperature,  $T_i$ , of the combustion chamber to be heated to a maximum of 398 K, thus achieving higher final compressed gas temperatures.

Table 2  
Mixture compositions and temperature and pressure ranges for RCM study

Mix	$\phi$	MB	O <sub>2</sub>	N <sub>2</sub>	Ar	Temperature range (K)	Pressure (atm)
1	1.00	0.0313	0.2034	0.7653	–	694–782	20, 10
2	1.00	0.0313	0.2034	0.3826	0.3827	799–859	20, 10
3	1.00	0.0313	0.2034	–	0.7653	825–949	20, 10
4	0.50	0.0313	0.4068	0.5619	–	640–772	20, 10
5	0.50	0.0313	0.4068	–	0.5619	747–922	20, 10
6	0.33	0.0313	0.6102	–	0.3585	694–842	20, 15, 10
7	0.50	0.0159	0.2067	0.7774	–	657–817	40, 20, 10
8	0.50	0.0159	0.2067	0.3887	0.3887	755–929	40, 20, 10
9	0.50	0.0159	0.2067	–	0.7774	893–936	40, 20, 10

### 2.2.2. Pressure control

Variations in the mixture composition and in particular in the initial temperature result in inconsistent compressed gas pressures for a consistent initial test gas pressure. Therefore, in order to reach a consistent compressed gas pressure,  $P_C$ , the initial test gas pressure,  $P_i$ , needed for a specific mixture was calculated using the *adiabatic compression/expansion* facility in the GasEq [23] application. Before compression, the test gas mixture was introduced into the preheated combustion chamber from the mixing tank to a known  $P_i$ . The test gas mixture was allowed to equilibrate to the temperature of the combustion chamber for two minutes and was then compressed by simultaneous movement of the twin opposed pistons.

A pressure transducer (Kistler 603B) flush with the combustion chamber wall was used to monitor the change in pressure with time. The signal from the pressure transducer was passed through a charge amplifier (Kistler Type 5001) before being recorded by an oscilloscope (Nicolet TDS). The pressure transducer and charge amplifier were both regularly calibrated.

The ignition delay time, defined as the time from the end of compression to the maximum rate of pressure rise during ignition, was measured using two vertical cursors on the oscilloscope.

Experimentally measured ignition delay times shorter than 50 ms were reproducible to within  $\pm 4.0$  ms over two to four experiments for each condition, while those longer than 50 ms were less reproducible. The time for compression is very short (16 ms), with 90% of the temperature rise occurring in the final 2 ms of the compression stroke. Thus, heat losses during compression are small.

However, the period following compression initially experiences a large amount of heat loss owing to the swirl experienced within the chamber due to the piston stroke. After this period, heat losses continue from the core gas but at a much decreased rate. If the ignition delay times are short, that is, less than 80 ms, heat losses have only a small effect on the unfolding chemistry. However, as the ignition delay times

increase, the heat losses to the walls have a greater impact on the experimental results. Even though ignition delays were observed up to 200 ms following compression, delays greater than 50 ms were found to be less consistent.

The compressed gas temperature,  $T_C$ , was calculated from  $T_i$ ,  $P_i$ , reactant composition, and the experimentally measured  $P_C$  (defined as the maximum measured pressure immediately after compression) from the equation

$$\ln\left(\frac{P_C}{P_i}\right) = \int_{T_i}^{T_C} \frac{\gamma}{\gamma - 1} \frac{dT}{T}. \quad (1)$$

Equation (1) assumes frozen chemistry and uses the temperature-dependent specific heat ratio,  $\gamma$ . The measured ignition delay times are then plotted as a function of inverse temperature in order to obtain overall reactivity profiles of the methyl butanoate mixtures.

### 2.2.3. Experimental error

As discussed above, the reproducibility of longer ignition delay times is dependent on the homogeneity of the temperature field in the compressed volume. The temperature field becomes less homogeneous with time and as such there is typically much larger scatter on the y-axis for lower temperature and longer ignition delay times.

The error in the determination of the important  $T_C$  can be quantified. The moiety in Eq. (1) with the largest uncertainty is the value of  $P_C$ . The error in the determination of  $P_C$  is estimated to be at most  $\pm 0.5$  atm. If this uncertainty is applied to Eq. (1), the corresponding average error in  $T_C$  is  $\approx \pm 6$  K.

## 3. Kinetic model

The detailed chemical kinetic mechanism presented in this study has been extensively modified from our previous work [15] and consists of 275 species and 1545 reactions. Due to the size of the model, here we will describe only modifications to important reaction classes and important individual reactions. The full kinetic model and associated thermochemistry and transport parameters are available for download at <http://www.nuigalway.ie/chem/combust.htm#meccs>.

Since no low-temperature reactivity was observed, we have not included low-temperature chemistry to describe the isomerization of alkylperoxyl radicals to hydroperoxyl alkyl radicals and so on. In addition to decomposition, we have considered only the reactions of MB alkyl radicals with molecular oxygen and the  $\text{RO}_2$ -type species.

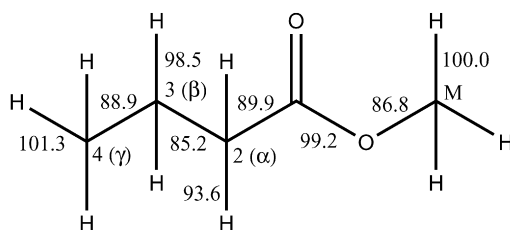


Fig. 1. Methyl butanoate bond enthalpies at 298 K/kcal mol<sup>-1</sup>.

### 3.1. Transport parameters

Transport parameters have been estimated for species of the MB submechanism based on the parameters of species with similar molecular mass. All other transport parameters are those used by Curran et al. [29].

### 3.2. Thermochemistry

It has been several years since Fisher et al. [6] published their study on MB oxidation; therefore the thermochemistry of all species produced by homolytic cleavage of MB has been reestimated. The thermodynamic properties for the relevant radicals and stable parents were generated in the form of NASA polynomials using Benson's [30] group additivity method employing THERM [31] with updated H/C/O and bond dissociation groups [32,33]. These calculations result in a set of bond enthalpies for MB, as shown by Fig. 1.

These values are in substantial agreement with the work of El-Nahas et al. [17], and some important differences were found in comparison with the estimates of Fisher et al.:

- the bond enthalpy of the C–H bond  $\alpha$  to the carbonyl group has been reduced to 93.6 kcal mol<sup>-1</sup> from 96.2 kcal mol<sup>-1</sup>;
- the bond enthalpy of the  $n\text{C}_3\text{H}_7\text{C}(\text{O})\text{O}-\text{CH}_3$  bond has been reduced to 86.8 kcal mol<sup>-1</sup> from 101.2 kcal mol<sup>-1</sup>;
- the bond enthalpy of the  $n\text{C}_3\text{H}_7-\text{C}(\text{O})\text{OCH}_3$  bond has been reduced to 89.9 kcal mol<sup>-1</sup> from 92.0 kcal mol<sup>-1</sup>.

#### 3.2.1. $\text{H}_2$ , $\text{C}_3$ , $\text{C}_4$ submechanisms

The nature of a detailed chemical kinetic mechanism is intrinsically hierarchical. Since it has been a number of years since the work of Fisher et al. [6], it was necessary to update the submechanisms on which the MB chemistry was added.

- The  $\text{H}_2/\text{O}_2$  submechanism has been replaced with that published by O'Conaire et al. [34].

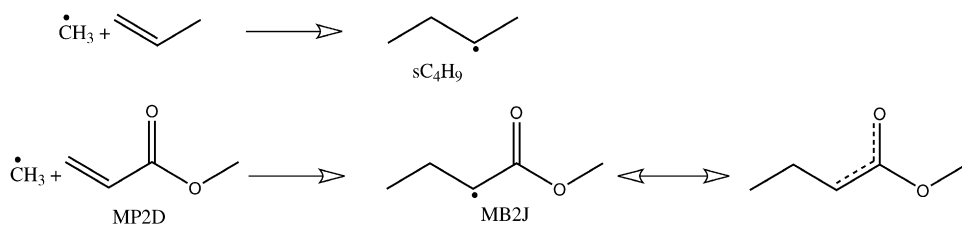


Chart 1.

- The  $\text{C}_3$  submechanism has been replaced with that recently published by Petersen et al. [35].
- An original  $\text{C}_4$  submechanism has been developed and added based on the work of Curran et al. [29,36] to account for  $\text{C}_4$  species observed in the experiments of Gail et al. [12] and Sarathy et al. [13].

### 3.2.2. Unimolecular fuel decomposition

The high-pressure-limit rate constant expressions for all unimolecular decomposition reactions involving C–C and C–O bond fission have been reestimated, resulting in an average decrease of one-third in the frequency factor from the original expressions of Fisher et al. As described below, these rate expressions are estimated in the reverse radical–radical recombination direction, which is a barrierless process, with the forward expression, unimolecular fuel decomposition, calculated from thermochemistry via microscopic reversibility.

These new expressions have essentially been adjusted and optimized by comparing the model predictions to our experimental ignition delay times. As discussed in the following sections, the accurate prediction of data in the high-temperature regime is extremely dependent on the correct assignment of the unimolecular fuel decomposition reactions. We recognize that this is a general correction, but currently no other literature data (either measurement or calculation) exist to allow a better discrimination as to the relative rates of the decomposition channels.

These rate constants have also been treated using quantum Rice–Ramsperger–Kassel theory with a master equation analysis [37] in order to account for pressure falloff. Moreover, the resulting rate expressions were fitted using the conventional nine-parameter Troe formalism.

The rate constants for alkyl and alkoxy radical decomposition have been estimated taking into account the work of Curran [38], who recently published a review and an interpretation of rate constant estimation for  $\text{C}_1$  to  $\text{C}_4$  alkyl and alkoxy radical decomposition.

We estimate the rate constant for the reaction  $\dot{\text{R}} \rightarrow \dot{\text{P}} + \text{Q}$  in the reverse exothermic direction ( $\dot{\text{P}} + \text{Q} \rightarrow \dot{\text{R}}$ ) and allow the forward rate constant ( $\dot{\text{R}} \rightarrow \dot{\text{P}} + \text{Q}$ ) to be calculated from the equilibrium constant using the

principle of microscopic reversibility [39]. This approach allows us to avoid the additional complication of the enthalpy of reaction.

There are almost no kinetic data available for the oxygenated radicals formed during MB decomposition [40]. A key aspect of this study has been determining the most appropriate way of treating reactions involving those types of radicals. We have found it necessary to treat all resonantly stabilized radicals formed during the oxidation of MB as behaving in a fashion similar to the vinyl radical, and our rate constants for reactions involving these radicals have been estimated using analogous reactions involving the vinyl radical.

The following individual reactions were found to be of particular importance and are worthy of a more detailed description:

(1)  $\dot{\text{C}}\text{H}_3 + \text{MP2D} \rightarrow \text{MB2J}$ : a rate constant of  $1.00 \times 10^{13} \exp(-14,000 \text{ cal mol}^{-1}/RT) \text{ cm}^3 \text{ mol}^{-1} \text{ s}^{-1}$ , based on the rate expression recommended by Curran for  $\dot{\text{C}}\text{H}_3 + \text{C}_3\text{H}_6 \rightarrow s\dot{\text{C}}_4\text{H}_9$ , has been used (see Chart 1).

We have modified Curran's estimate for the formation of  $s\dot{\text{C}}_4\text{H}_9$  to account for the resonance stabilization to the radical site of the MB2J species due to the presence of the carbonyl group. The difference in the two expressions corresponds to an increase in the activation energy of this process by  $2 \text{ kcal mol}^{-1}$  for the decomposition of MB2J relative to  $s\dot{\text{C}}_4\text{H}_9$ .

(2)  $n\text{C}_3\text{H}_7\dot{\text{C}}\text{O} + \text{CH}_2\text{O} \rightarrow \text{MBMJ}$ : we have assumed the  $n\text{C}_3\text{H}_7\dot{\text{C}}\text{O}$  radical to behave in a fashion similar to the vinyl radical (see Chart 2).

In light of this we recommend a rate constant based on the work of Rauk et al. [41], who performed calculations at the B3-LYP/6-31G(d) and CBS-RAD levels of theory to determine rate constants for the addition reactions of, among other species, the vinyl radical to a host of carbonyl compounds. Rauk et al. calculated an A-factor of  $3.89 \times 10^{11} \text{ cm}^3 \text{ mol}^{-1} \text{ s}^{-1}$  and an activation of  $2.5 \text{ kcal mol}^{-1}$  for the addition of a vinyl radical to the carbon atom in formaldehyde. To our knowledge there is an absence of kinetic data to describe the addition of the vinyl radical to the oxygen atom of carbonyl compounds. However, Hippler and Viskolcz [42] have carried out a study of the competi-



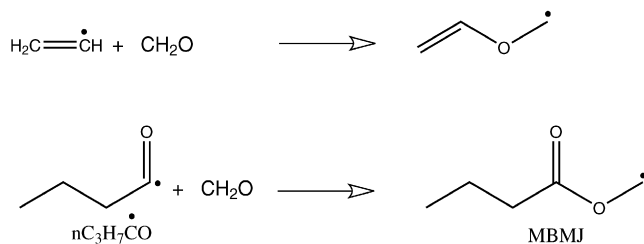


Chart 2.

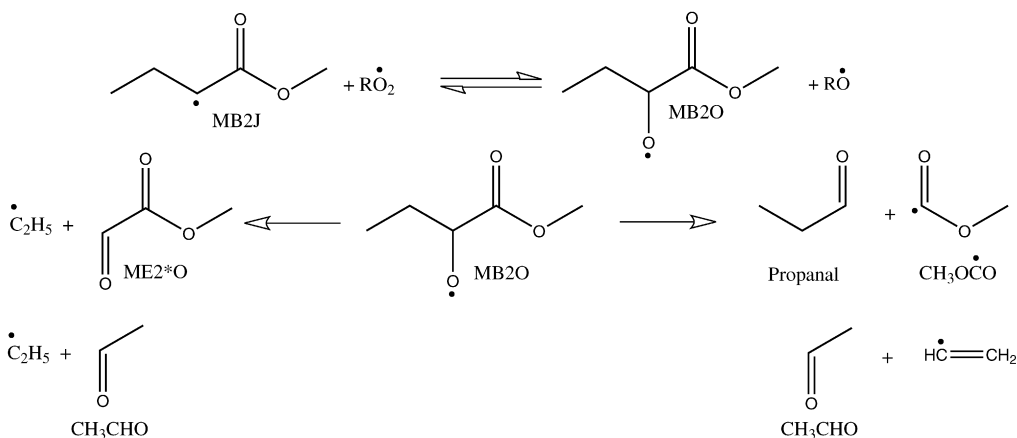


Chart 3.

tion between alkyl radical addition to carbonyl bonds and hydrogen abstraction. Using (G3(MP2)//B3LYP) ab initio molecular orbital theory, they determined the barrier height for addition of an alkyl radical to the oxygen atom of a carbonyl to be consistently approximately  $8.4 \text{ kcal mol}^{-1}$  higher than the barrier for addition to the carbon atom.

Taking the work of Rauk et al. and Hippler and Viskolcz into account, we have generated a rate constant of  $3.89 \times 10^{11} \exp(-10,900 \text{ cal mol}^{-1}/RT) \text{ cm}^3 \text{ mol}^{-1} \text{ s}^{-1}$  for the addition of the  $\text{nC}_3\text{H}_7\dot{\text{C}}\text{O}$  radical to the oxygen atom of formaldehyde. The reverse reaction, the decomposition of the MBMJ radical has a rate constant of  $1.64 \times 10^{22} T^{-2.33} \exp(-31,950 \text{ cal mol}^{-1}/RT) \text{ cm}^3 \text{ mol}^{-1} \text{ s}^{-1}$ .

(3) The MB2O radical is formed by the reaction of the MB2J radical with an  $\text{RO}_2^\bullet$  type species. The subsequent decomposition of this species can proceed via two pathways: by  $\beta$ -scission of the C–C bond  $\alpha$  to the carbonyl to form  $\text{CH}_3\text{OCO}^\bullet$  and propanal, or alternatively by  $\beta$ -scission of the C–C bond  $\beta$  to the carbonyl to form an ethyl radical and a keto ester (see Chart 3).

A rate expression of  $3.33 \times 10^{10} \exp(-1497 \text{ cal mol}^{-1}/RT) \text{ cm}^3 \text{ mol}^{-1} \text{ s}^{-1}$  is used for the addition of an ethyl radical to the carbon atom of the terminal carbonyl group of  $\text{ME2}^*\text{O}$ . The frequency factor of the above expression is taken from Curran's [38] rec-

ommendation for  $\dot{\text{C}}_2\text{H}_5 + \text{CH}_3\text{CHO} \rightarrow \text{sC}_4\text{H}_9\dot{\text{O}}$  and the activation energy is calculated using an expression presented by Curran,

$$E_A = (1.956[\text{IP}] - 6.45) + 0.485\Delta H_f,$$

where IP is the ionization potential of the alkyl radical in electron volts and  $E_A$  and  $\Delta H_f$  are in  $\text{kcal mol}^{-1}$ , which correlates the activation energy with the ionization potential of the radical adding group.

For the addition of  $\text{CH}_3\text{OCO}^\bullet$  to the carbon atom of the carbonyl group in propanal, we use a rate expression of  $9.33 \times 10^{10} \exp(-3943 \text{ cal mol}^{-1}/RT) \text{ cm}^3 \text{ mol}^{-1} \text{ s}^{-1}$ , which is the expression calculated by Rauk et al. [41] for the addition of a vinyl radical to acetaldehyde ( $\text{CH}_3\text{CHO}$ ) to yield  $\text{CH}_2\text{CHCH}\dot{\text{O}}\text{CH}_3$ .

### 3.2.3. Hydrogen abstraction from fuel

The rate constants for hydrogen atom abstraction from MB and all major intermediates were based on a series of rules depending on the identity of the abstracting radical ( $\dot{\text{H}}$ ,  $\text{HO}_2^\bullet$ ,  $\dot{\text{O}}\text{H}$ , etc.) and on the nature of the carbon atom to which the hydrogen atoms are bound, that is, primary, secondary, or tertiary atoms.

We have used the rate constants for abstraction recommended by Orme et al. [43] in a study of methyl cyclohexane oxidation. An exception to this is the treatment of hydrogen abstraction by  $\text{HO}_2^\bullet$ , where we have decreased the values of the frequency fac-

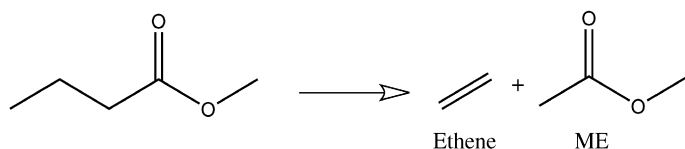


Chart 4.

tor from Orme et al. by multiplication by a factor of 0.85 to improve model agreement with experiments at low to intermediate temperature (800–900 K). To be consistent, the rate expressions for the similar  $\text{CH}_3\text{O}_2$  radical have been treated identically. Hydrogen abstraction takes place from MB from four sites. From Fig. 1 it is clear that the computed C–H bond enthalpies of the carbon atom  $\alpha$  to the carbonyl and those of the carbon atom at the methyl position are not the “standard” values typical of primary, secondary, or tertiary carbon atoms. Hence we have treated hydrogen abstraction from the site  $\alpha$  to the carbonyl as being from a tertiary carbon atom, and from the site at the methyl position as being from a secondary carbon atom, reflecting their C–H bond enthalpies.

A number of additional reaction channels have been added; these include

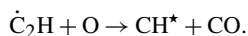
- A six-centered elimination reaction from MB producing methyl ethanoate (ME) and ethene, through an enol–keto isomerization (see Chart 4). The rate expression for this elimination reaction is derived from the frequency factor recommended by Blades and Sandhu [44] and the activation energy has been assigned a value of  $68 \text{ kcal mol}^{-1}$  from our earlier work by El-Nahas et al. [17]. This value for the activation energy is in good agreement with the estimate of  $70 \text{ kcal mol}^{-1}$  by Blades and Sandhu. ME consumption chemistry analogous to that of MB has also been included.
- A more comprehensive consumption pathway of methyl propenoate including a full array of hydrogen abstraction reactions from all positions along the molecule has been included.

#### 4. Computational simulations

The modeling computations in this study were carried out using the HCT [45] modeling code for the jet-stirred reactor, flow reactor, shock tube, and rapid compression machine environments. The Oppdiff module of the application Chemkin [46] was used to simulate the opposed-flow diffusion flame environment.

The fundamental modeling assumptions used in comparing the kinetic calculations with experiments are as follows:

Shock tube simulations are zero-dimensional and begin at the onset of the reflected shock period, assuming constant volume and homogeneous adiabatic conditions behind the reflected shock wave. The reflected shock pressure ( $P_5$ ) and temperature ( $T_5$ ) are input as the initial pressure and temperature respectively, and we define the simulated ignition delay time as the time at which the maximum value of  $[\dot{\text{C}}_2\text{H}] \times [\dot{\text{O}}]$  occurs. We have not included any reactions in the current model to account for emission from the electronically excited  $\text{CH}^*$  species, which we measure experimentally. Therefore, in order to simulate our shock tube ignition delay times, we use the relation established by Horning et al. [47], which states that the rate of emission from  $\text{CH}^*$  can be inferred from the rate of production of  $\text{CH}^*$ :



The flow reactor was simulated using a zero-dimensional model assuming constant-pressure, adiabatic conditions. The jet-stirred reactor is simulated as a homogeneous, constant-volume reactor and is assumed to be at constant temperature and pressure, with a prescribed influx of fresh reactants such that the residence time is constant within the reactor.

The RCM environment is characterized by two distinct stages of pressure and temperature: first, a rapid rise in temperature and pressure due to compression, and second, the postcompression phase, which is characterized by a drop in pressure as the test gas loses heat to the cold reaction chamber walls. Due to these changing levels of temperature and pressure, the combustion environment encountered in a rapid compression machine is among the most challenging to simulate [48].

During a reactive experiment the extent of the adiabatic cooling can be masked by heat release due to the chemical reactions of combustion. Successful simulation of the RCM environment requires an accurate treatment of this heat loss. A number of approaches have been used to simulate this complex environment [49].

In this study we have chosen the technique of “heat loss mapping” as recently implemented in simulating data obtained for propane oxidation in the NUI, Galway RCM by Gallagher et al. [50] and used successfully by Mittal et al. [51,52], as well as by Silke et al. [53], in very recent studies. As detailed



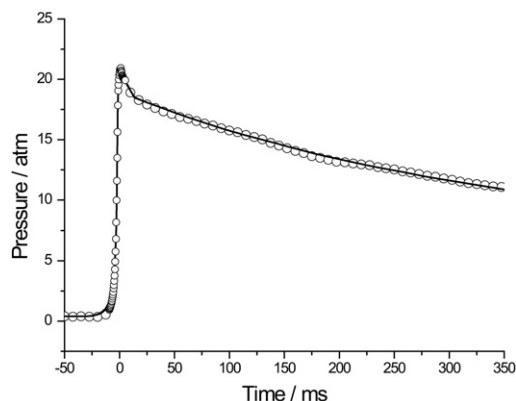


Fig. 2. Experiment  $\circ$  vs simulation — of an MB:N<sub>2</sub>:Ar 0.0313:0.4068:0.5619 unreactive compression.

by Mittal and Sung [52], using creviced piston heads allows for the assumption of an adiabatic core gas. This technique applies a volume expansion to simulate the reduction in pressure due to the heat loss of the boundary layer to the reaction chamber walls.

HCT treats the RCM as a homogeneous reactor (zone) with a rigid right boundary and a left boundary that moves at a specified velocity (piston velocity). A positive piston velocity indicates compression and a decrease in volume, while a negative velocity corresponds to an expansion process in which the volume increases. All experiments were simulated in three phases: (i) the compression phase, (ii) a phase immediately after the end of compression where the greatest drop in pressure was observed in each experiment, and (iii) a phase after this to infinite time with a more constant, and lesser, pressure decrease. Phases (ii) and (iii) were simulated as an adiabatic expansion process, with a greater expansion in phase (ii) compared to phase (iii).

We use HCT and the full chemical kinetic model to determine the piston velocity which reproduces the experimental pressure profile of an unreactive experiment where the value of  $\gamma$  is the same as an equivalent reactive mixture. This is achieved by replacing the O<sub>2</sub> fraction of the mixture with N<sub>2</sub>. Fig. 2 shows a comparison of experiment and simulation of an unreactive compression. Thereafter, we apply this physical model to the corresponding reactive mixture in order to test the chemical model.

## 5. Results and discussion

### 5.1. Shock tube

Shock tube ignition delay times for MB/O<sub>2</sub>/Ar mixtures were measured over the temperature range 1250–1706 K, at reflected shock pressures of 1.0 and

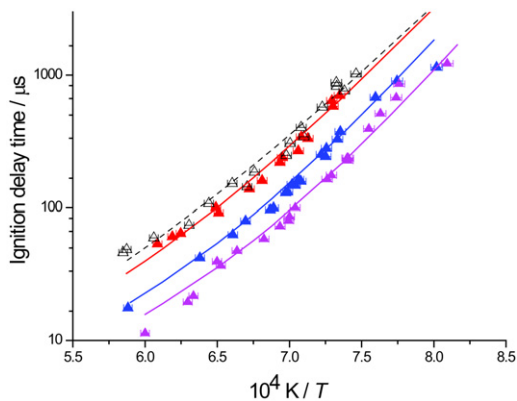


Fig. 3. MB ignition delay times at a reflected shock pressure of 1 atm with error bars of  $\pm \approx 7$  K. 1.5% MB,  $\phi = 1.5$   $\triangle$  ---; 1.0% MB,  $\phi = 1.0$   $\triangle$  —; 1.0% MB,  $\phi = 0.5$   $\triangle$  —; 1.0% MB,  $\phi = 0.25$   $\triangle$  —. (For interpretation of the references to color in this figure legend, the reader is referred to the web version of this article.)

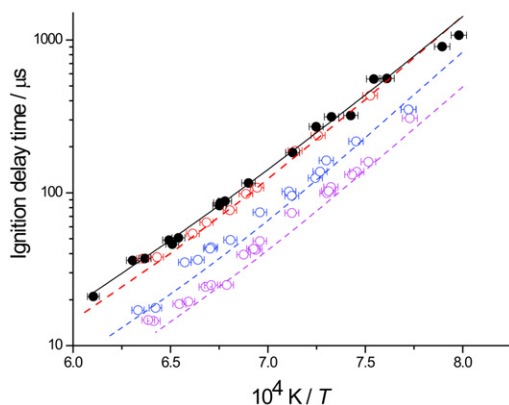


Fig. 4. MB ignition delay times at a reflected shock pressure of 4 atm with error bars of  $\pm \approx 7$  K. 1.5% MB,  $\phi = 1.5$   $\bullet$  —; 1.0% MB,  $\phi = 1.0$   $\circ$  ---; 1.0% MB,  $\phi = 0.5$   $\circ$  ---; 1.0% MB,  $\phi = 0.25$   $\circ$  ---. (For interpretation of the references to color in this figure legend, the reader is referred to the web version of this article.)

4.0 atm ( $\pm 0.1$  atm) and equivalence ratios of 1.5, 1.0, 0.5, and 0.25. Figs. 3 and 4 show experimental ignition times (symbols) and simulations (lines).

The effect of equivalence ratio on the ignition delay time is in line with previous autoignition studies of hydrocarbons [21,43] and oxygenates [15] in the high-temperature regime. Only a slight increase in induction time is observed as the MB concentration increases from 1.0% to 1.5% at a constant O<sub>2</sub> concentration of 6.5%. The effect of increased O<sub>2</sub> concentration is more dramatic, as the O<sub>2</sub> concentration is increased from 6.5% to 13.0% to 26.0% with a constant MB concentration of 1.0% the ignition delay times show a significant reduction at both pressures

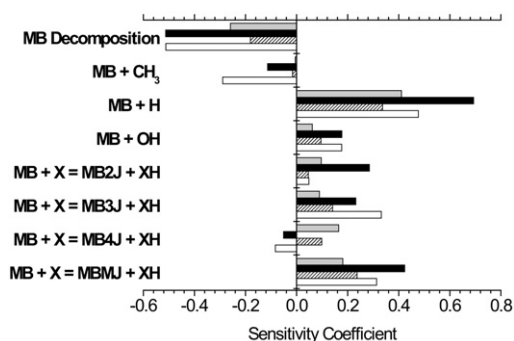


Fig. 5. Sensitivity coefficients for shock tube simulations of 1.0% MB, in Ar at 1 atm: (white) 1300 K,  $\phi = 1.0$ ; (hashed) 1600 K,  $\phi = 1.0$ ; (black) 1300 K,  $\phi = 0.25$ ; (gray) 1600 K,  $\phi = 0.25$ .  $\tau$  is the sensitive parameter.

studied, Figs. 3 and 4. The observed positive power dependence of fuel concentration, and the negative power dependence of  $O_2$  concentration are consistent with previous shock tube studies over similar regimes for hydrocarbon fuels [22]. Modeling simulations of the shock tube conditions accurately reproduce the experimental data, with the influence of temperature, pressure and equivalence ratio well captured.

A sensitivity analysis was performed on the kinetic model to elucidate the important channels of reaction for MB under these shock tube conditions. The brute force technique [54] was employed by multiplying the forward and reverse rate constants of a reaction or reaction class by a factor of 2 and noting the effect on the computed ignition delay time. We define the sensitivity coefficient,  $\sigma$ , as  $\sigma = (\tau' - \tau)/\tau$ , where  $\tau$  is the original delay and  $\tau'$  is the delay time calculated using the adjusted rate constant. Thus, a positive sensitivity coefficient represents a longer ignition time, indicating that this reaction impedes reactivity and a negative coefficient indicates a shorter ignition time, indicating that this reaction promotes reactivity. Sensitivity coefficients normalized to a value of one are shown in Figs. 5 and 6.

As we identified in our earlier work on methyl butanoate, shock tube ignition times are extremely sensitive to the rate of unimolecular fuel decomposition. These are reactions that occur by homolytic bond cleavage producing two reactive radicals from a stable parent. Thus our treatment of this reaction class is largely significant in attaining agreement with experiment. From the sensitivity analysis (Fig. 5), it can be seen how important this class of reaction is.

We also note the importance of hydrogen abstraction from MB by hydrogen (H) atoms (Fig. 5). This is another important modification made to the model to attain agreement with shock tube ignition times. We set the rates of hydrogen abstraction from MB close to the highest reasonable values allowed, as the C–H

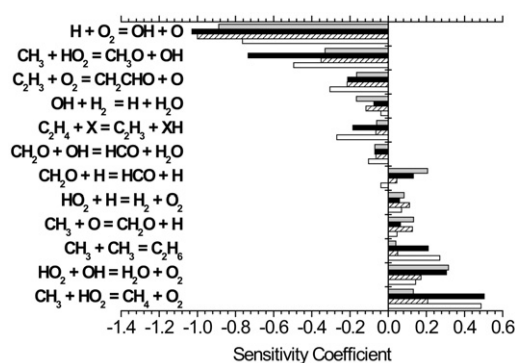


Fig. 6. Sensitivity coefficients for shock tube simulations of 1.0% MB, in Ar at 1 atm: (white) 1300 K,  $\phi = 1.0$ ; (hashed) 1600 K,  $\phi = 1.0$ ; (black) 1300 K,  $\phi = 0.25$ ; (gray) 1600 K,  $\phi = 0.25$ .  $\tau$  is the sensitive parameter.

bond enthalpies at the “M” and “2” positions along the fuel molecule are not of standard values. The most important chain branching reaction under high temperature conditions is  $\dot{H} + O_2 \rightarrow \dot{O} + \dot{O}H$  (Fig. 6), as this reaction is the dominant radical chain branching process. Abstraction from MB by  $\dot{H}$  atoms is very sensitive under shock tube conditions because it competes with this process and thus inhibits reactivity.

To further understand the chemistry controlling the autoignition of MB under shock tube conditions, an analysis of the chemical flux was carried out for a stoichiometric mixture of 1% MB in Ar at 1 atm and 1600 K. The simulation was frozen at 50% fuel consumption, corresponding to a time of 9.7  $\mu s$  and a temperature of 1546 K with a simulated ignition delay of 62.0  $\mu s$  at this condition. It was found that the majority of MB is consumed by hydrogen abstraction, with  $\dot{H}$  atoms (58.3%),  $\dot{O}H$  radicals (16.8%),  $\dot{C}H_3$  radicals (3.5%), and O atoms (5.0%) responsible. Unimolecular fuel decomposition reactions account for the remaining 16.4%. The proportions in which the primary alkyl radicals are formed are given in Chart 5.

Due to the relatively high temperatures in the shock tube, addition of alkyl radicals to molecular oxygen and abstraction of an oxygen atom from the  $RO_2$  type species are not competitive with alkyl radical decomposition reactions. However, as we discuss later, this is not the case at lower temperatures for the RCM experiments.

The fuel alkyl radical formed in the largest quantity is MB2J and there are a number of channels through which it can decompose, but the production of MP2D and a methyl radical dominates (see Chart 6).

Under these conditions MB2J decomposition produces 35% of all  $\dot{C}H_3$  radical present. Fig. 6 shows us that reactions involving the  $\dot{C}H_3$  radical are important, particularly so at 1300 K. Analysis of  $\dot{C}H_3$

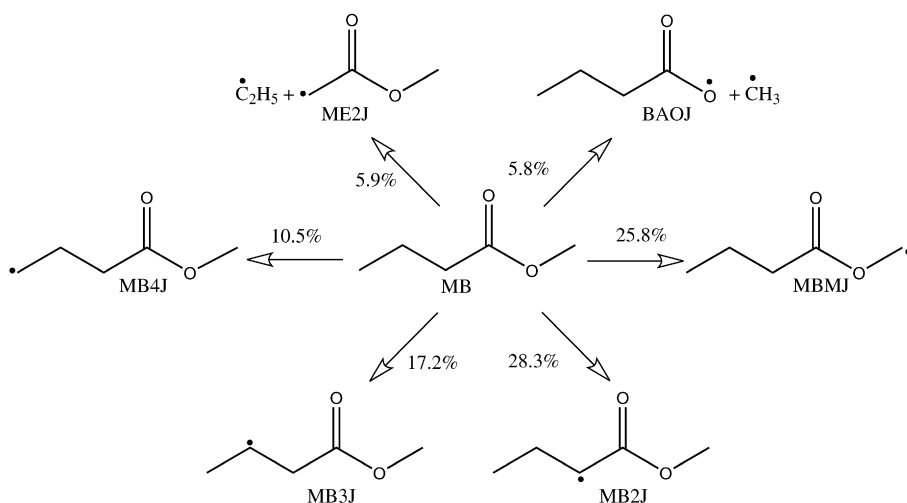


Chart 5.

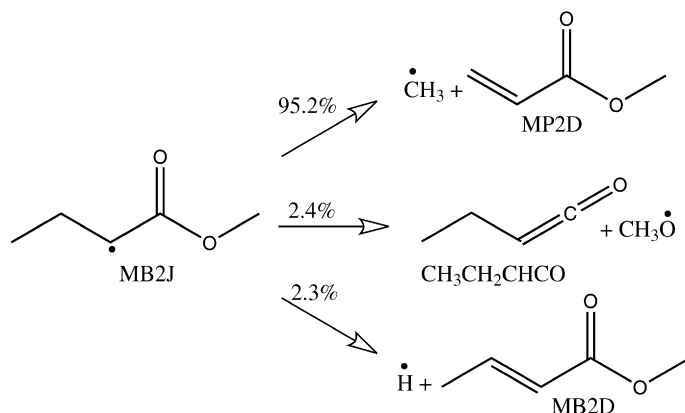


Chart 6.

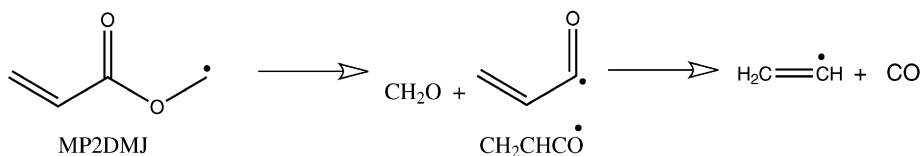


Chart 7.

radical consumption under these conditions shows that the reaction  $\dot{\text{C}}\text{H}_3 + \text{H}\dot{\text{O}}_2 \rightarrow \text{CH}_3\dot{\text{O}} + \dot{\text{O}}\text{H}$  is the dominant channel, consuming 46% of all  $\dot{\text{C}}\text{H}_3$  radicals present. Competing for  $\dot{\text{C}}\text{H}_3$  radicals with this process are two radical chain termination processes,  $\dot{\text{C}}\text{H}_3 + \dot{\text{C}}\text{H}_3 \rightarrow \text{C}_2\text{H}_6$  and  $\dot{\text{C}}\text{H}_3 + \text{H}\dot{\text{O}}_2 \rightarrow \text{CH}_4 + \text{O}_2$ , which account for 12% and 11% of  $\dot{\text{C}}\text{H}_3$  radical consumption, respectively. This competition for  $\dot{\text{C}}\text{H}_3$  radical explains the sensitivity coefficients in Fig. 6. The radical chain termination reactions slow the reactivity and therefore exhibit positive sensitivity coefficients. On the other hand, the radical chain propaga-

tion process shows a negative sensitivity coefficient as it converts a  $\text{H}\dot{\text{O}}_2$  radical into a more reactive  $\dot{\text{O}}\text{H}$  radical and by doing so reduces  $\dot{\text{C}}\text{H}_3$  radical chain termination and thus increases the reactivity of the system.

MP2D is subsequently consumed largely by hydrogen abstraction reactions, mainly by  $\dot{\text{H}}$  atoms. The resulting radicals undergo intermolecular isomerization or form a stable alkyne and a reactive radical or, in the case of MP2DMJ, formaldehyde and a reactive radical,  $\text{CH}_2\text{CHC}\dot{\text{O}}$ , which dissociates to carbon monoxide and a vinyl radical (see Chart 7).

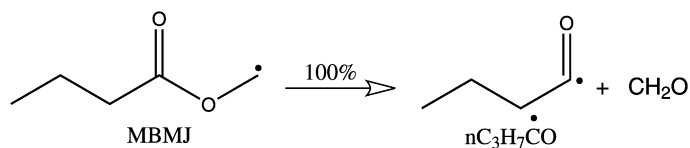


Chart 8.

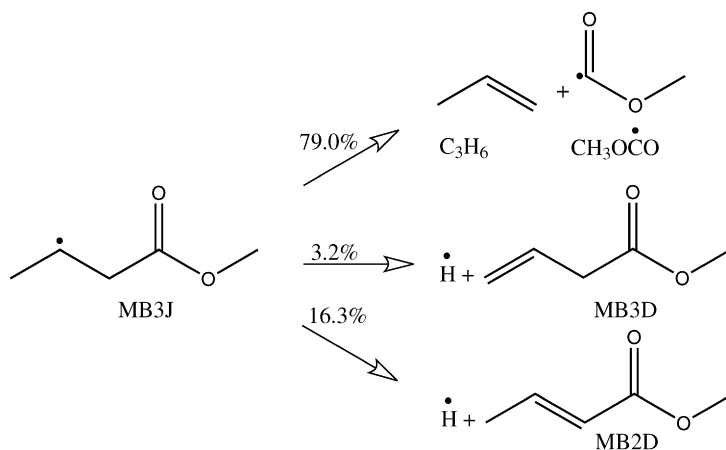


Chart 9.

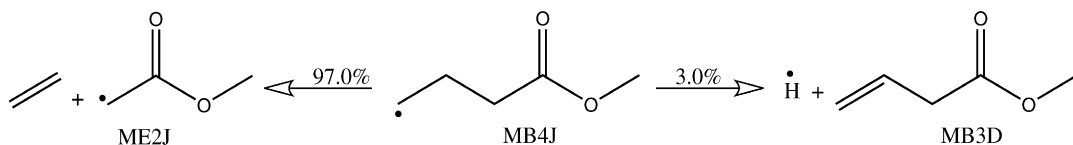


Chart 10.

MBMJ is the second most abundant fuel alkyl radical and undergoes  $\beta$ -scission to generate formaldehyde and the  $nC_3H_7\dot{C}O$  radical. This reaction dominates the alternative isomerization reactions, and accounts for all MBMJ consumption under these conditions (see Chart 8).

MB3J preferentially decomposes via  $\beta$ -scission of the most labile bond available to the radical. Although  $\beta$ -scission of the C–H bond  $\alpha$  to the carbonyl is competitive,  $\beta$ -scission of the C–CO bond producing propene dominates (see Chart 9).

From Fig. 5 it can be seen that hydrogen abstraction from all sites on the molecule has the effect of increasing the ignition delay. This is because  $\dot{H}$  atom is the main abstractor and because of the aforementioned competition between this process and the reaction of  $\dot{H} + O_2 \rightarrow \dot{O} + \dot{O}H$ . Interestingly this effect is not observed for hydrogen abstraction from the terminal position on the MB alkyl chain, where abstraction increases reactivity at 1300 K and decreases reactivity at 1600 K respectively (Fig. 5). This attribute is due to the formation of ethene from the MB4J radical. MB4J decomposes similarly to MB3J via cleavage of

the weakest C–C bond available to the radical, with some competition from cleavage of a secondary C–H bond (see Chart 10).

Ethene subsequently undergoes hydrogen abstraction to form a vinyl radical, and the branching ratio of vinyl radical reaction with  $O_2$  is responsible for the changing effect of abstraction from the terminal position on the MB alkyl chain with temperature. This is depicted in the following analysis of the chemical flux at 50% fuel consumption for conditions of 1% MB,  $\phi = 1.0$ , and 1 atm, where the percentages refer to total vinyl radical consumption (see Chart 11).

The activity of the chain branching pathway producing  $\dot{C}H_2CHO + \dot{O}$  is reduced at 1600 K relative to 1300 K, making the MB4J decomposition pathway less reactive at high temperatures relative to lower temperatures. In addition, Fig. 6 shows that vinyl radical production from ethene is significantly more sensitive at 1300 K than at 1600 K. Examination of ethene consumption under these conditions shows that at 1600 K 100% of ethene is converted to vinyl radicals via hydrogen abstraction, but at 1300 K this process accounts for only 80% of ethene con-

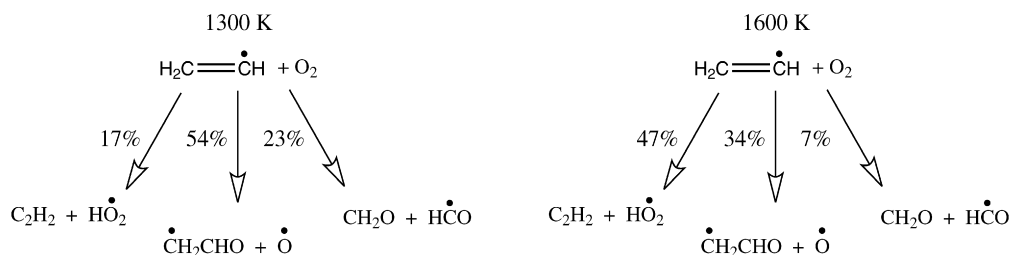


Chart 11.

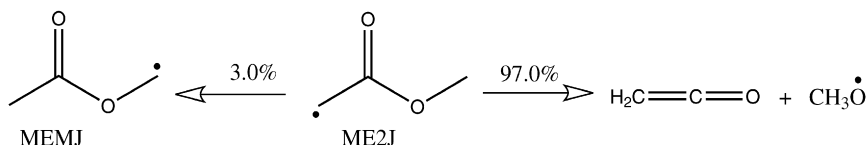


Chart 12.

sumption. The remaining 20% reacts with oxygen atoms via  $\text{C}_2\text{H}_4 + \dot{\text{O}} \rightarrow \dot{\text{C}}\text{H}_3 + \text{HCO}$ . An increase of a factor of 2 in the rate constants for hydrogen abstraction from ethene allows vinyl radical production to account totally for ethene consumption at 1300 K. Hence, the reactivity increases due to the chain-branching process of vinyl radical reaction with oxygen. Similar observations of the chemistry of the ethene–vinyl radical pathway were noted by Metcalfe et al. [15] in a study of ethyl propanoate oxidation over identical conditions.

The ME2J radical is produced directly from fuel decomposition, but also indirectly via hydrogen atom abstraction from MB through the decomposition of MB4J. At shock tube temperatures, isomerization of the ME2J radical to the MEMJ radical is not favored; rather, the ME2J radical decomposes to produce ketene and a methoxy radical (see Chart 12).

### 5.2. Rapid compression machine

The rapid compression machine was used to generate ignition delay data in the low-to-intermediate temperature range in order to complement the high-temperature shock tube ignition data. Figs. 7–10 show experimental rapid compression machine ignition delay times (symbols) as a function of inverse temperature, together with simulations (lines). Experimental data sets are consistent to within  $\pm 0.5$  atm and Arrhenius-like temperature dependence is observed.

The model shows reasonable agreement with experiment, considering the previously discussed approximations, which are necessary to simulate this sort of environment. The simulation procedure employed describes more accurately the postcompression environment of shorter ignition delay times compared to longer ignition times; at higher tempera-

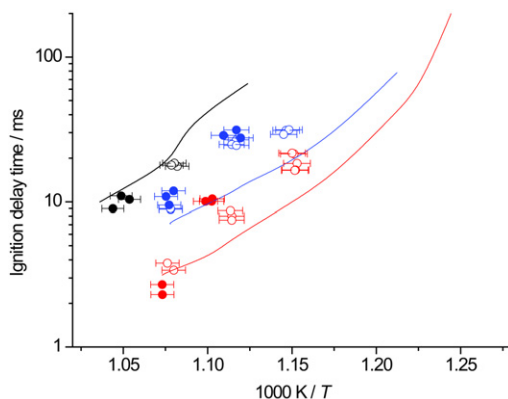


Fig. 7. RCM ignition delay times for 1.59% MB,  $\phi = 0.5$  with error bars of  $\pm \approx 6$  K. Filled symbols: diluent of 100% Ar; hollow symbols: diluent of 50%  $\text{N}_2$ /50% Ar. 10 atm  $\bullet$   $\circ$  —, 20 atm  $\bullet$   $\circ$  —, and 40 atm  $\bullet$   $\circ$  —. (For interpretation of the references to color in this figure legend, the reader is referred to the web version of this article.)

tures/shorter ignition delays the assumption of an adiabatic core gas is more valid, as there is less time for temperature inhomogeneities to develop. In addition, as discussed earlier, the aspect of temperature inhomogeneities affecting longer ignition delay times can be seen experimentally in the data, as there is more scatter in the data at lower temperatures.

There is considerable disagreement in the prediction of the temperature at which the onset of ignition occurs; the model predicts the onset of ignition at too low a temperature at low fuel concentrations (Fig. 7) and at too high a temperature for high fuel concentrations (Fig. 8).

Figs. 7–10 clearly show that not only does MB not show negative temperature coefficient (NTC) behavior, but it does not show extended reactivity over the

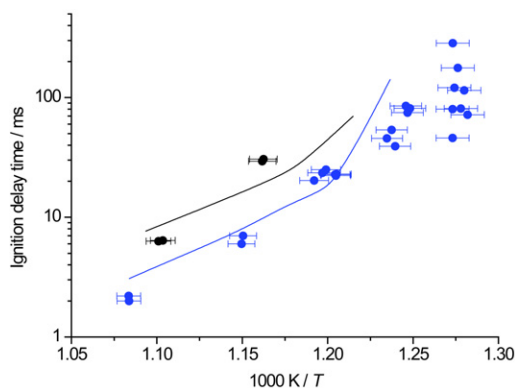


Fig. 8. RCM ignition delay times for 3.13% MB,  $\phi = 0.5$  with error bars of  $\pm \approx 6$  K. Diluent of 100% Ar. 10 atm ● — and 20 atm ● —. (For interpretation of the references to color in this figure legend, the reader is referred to the web version of this article.)

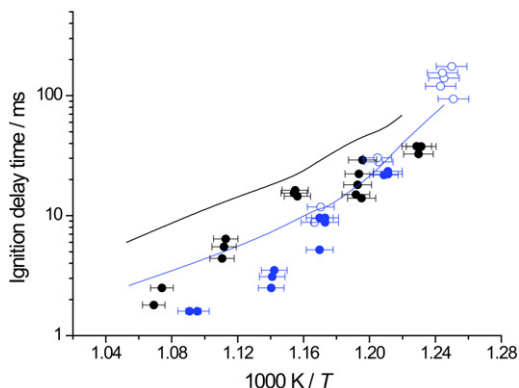


Fig. 9. RCM ignition delay times for 3.13% MB,  $\phi = 1.0$  with error bars of  $\pm \approx 6$  K. Filled symbols: diluent of 100% Ar; hollow symbols: diluent of 50%  $N_2$ /50% Ar. 10 atm ● — and 20 atm ● —. (For interpretation of the references to color in this figure legend, the reader is referred to the web version of this article.)

RCM temperature range (600–1000 K) under the conditions studied. Initially we examined the autoignition of MB at high pressures using a fuel concentration of 1.59% and an equivalence ratio of 0.5, conditions typical of numerous RCM studies on other hydrocarbons [48]. However, this mixture did not ignite at temperatures below 860 K. Thus, a second mixture was prepared with the fuel concentration doubled from 1.59% to 3.13%, retaining  $\phi = 0.5$ . Due to the low vapor pressure of MB (28.9 mbar at 18 °C) and the high fuel fraction present, the maximum achievable compressed gas pressure for this mixture was limited to 20 atm. Despite the lower  $P_C$ , the increased fuel fraction extended the point at which ignition occurred to 780 from 860 K. In an effort to further extend the reactivity of the fuel, mixtures of an equivalence ratio of

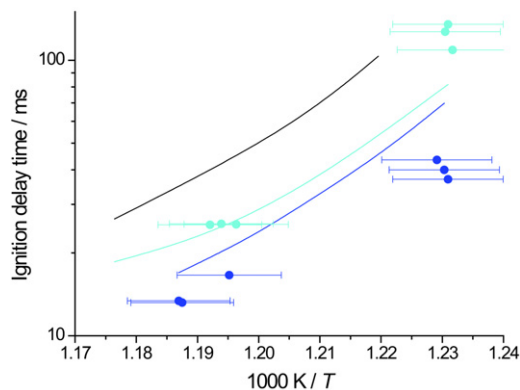


Fig. 10. RCM ignition delay times for 3.13% MB,  $\phi = 0.33$  with error bars of  $\pm \approx 6$  K. Diluent of 100% Ar. 10 atm no ignition —, 15 atm ● —, and 20 atm ● —. (For interpretation of the references to color in this figure legend, the reader is referred to the web version of this article.)

1.0 and 0.33 with a fuel fraction of 3.13% were tested (Figs. 9, 10). We observed no appreciable change in the temperature at which ignition occurs.

The influence of pressure is generally small. However, it does have a large influence on the temperature at which the onset of ignition occurs. The higher pressure experiments show ignition at temperatures lower than those at lower pressure.

The RCM data reported here and the flow reactor data of [11] disagree with the work of Fisher et al. [6], who predicted that NTC behavior should be observed for MB based on earlier observations of Parsons et al. [8]. They had reported that the rate of rise of pressure as a function of inverse temperature did not behave in an Arrhenius-type manner but went through an initial maximum value and then a reduction in the overall rate of reaction before the reactivity increased again. Although this observation seems to be characteristic of NTC behavior, Parsons et al. also measured the induction period over a limited temperature range of 555–610 K and found that their results followed the Arrhenius equation with no NTC character.

A sensitivity analysis of the kinetic model under RCM conditions is shown in Figs. 11 and 12. The same technique as described earlier was used with the sensitivity coefficients normalized to one. In addition, the sensitivity of the fuel alkyl radical +  $O_2$  = fuel alkylperoxyl radical pathway was tested for:

- (1) “A” denotes that the reaction class was removed completely;
- (2) “F” denotes a factor of 2 change in the forward rate constant, effecting a change in the equilibrium constant favoring the formation of alkyl radical +  $O_2$ ;



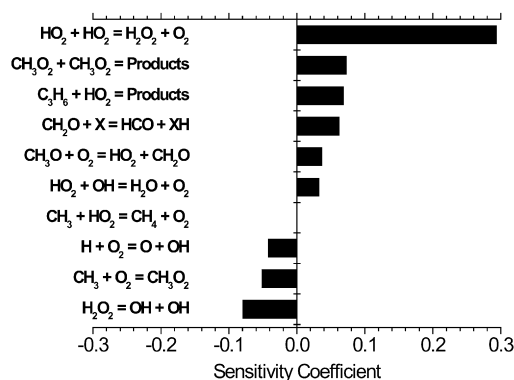


Fig. 11. Sensitivity coefficients for RCM ignition delays for a mixture of 3.13% MB,  $\phi = 0.5$  in Ar at 836 K and a compressed pressure of 20 atm.  $\tau$  is the sensitive parameter.

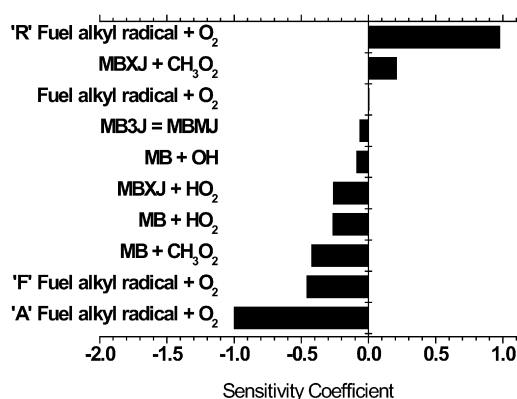


Fig. 12. Sensitivity coefficients for RCM ignition delays for a mixture of 3.13% MB,  $\phi = 0.5$  in Ar at 836 K and a compressed pressure of 20 atm.  $\tau$  is the sensitive parameter.

- (3) “R” denotes a factor of 2 change in the reverse rate constant, effecting a change in the equilibrium constant favoring the formation of alkylperoxyl radical.

Consideration of alkyl radical decomposition alone can not reproduce ignition delay times at temperatures below 850 K, with simulations consistently too fast compared to experiment, Fig. 13. The inclusion of the reaction of alkyl radical +  $O_2$  is clearly important in slowing the reactivity at lower temperatures, Fig. 12. However, its influence becomes diminished as the temperature increases and the equilibrium favors the formation of alkyl radical +  $O_2$ , Fig. 13. Similarly, the position of the equilibrium between reactants and products is just as sensitive, Fig. 12.

As the oxygen concentration is in large excess over the concentration of fuel alkyl radicals, both processes in the equilibrium are rapid, with the forward and reverse rates approximately equal. However,

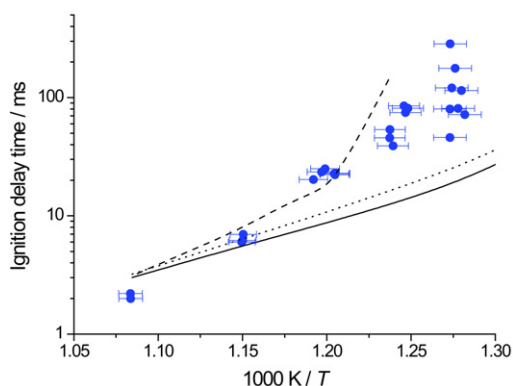


Fig. 13. RCM ignition delay times for 3.13% MB,  $\phi = 0.5$  at 20 atm with error bars of  $\pm \approx 6$  K. Diluent 100% Ar.  $\dot{R} + O_2/H\dot{O}_2/R\dot{O}_2$  pathway: --- included, ... omitted, and —  $\dot{R} + H\dot{O}_2/R\dot{O}_2$  only.

these low temperatures ( $< 850$  K) do allow a gradual buildup of alkylperoxyl radical.

The sensitivity analysis can largely be understood by examining the role that the  $HO_2$  radical plays in the unfolding chemistry. To explain the sensitivity analysis, a flux analysis was performed on the chemistry, occurring for a mixture of 3.13% MB,  $\phi = 0.5$  in Ar compressed to 836 K and 20 atm. The chemistry was frozen at a fuel concentration 50% of the original, corresponding to a time of 23.1 ms and a temperature of 982.4 K. The simulated ignition delay for these conditions is 23.3 ms (Fig. 14).

At these conditions hydrogen abstraction from MB by  $\dot{O}H$  radicals accounts for 70% of MB consumption. Of the remaining 30%, abstraction by  $H\dot{O}_2$  accounts for 10.2%, while  $\dot{H}$  atoms consume 8.8%, with abstraction by  $CH_3\dot{O}_2$  and O atom the only other minor contributors. As in the shock tube study, abstraction is marginally favored from the “2” position, Fig. 14.

Due to the wide-ranging temperatures in an RCM simulation, a complete description of chemical events is very difficult, with different reaction classes dominating as the temperature first decreases after compression and then rises to over 2000 K at ignition.

Each of the primary fuel alkyl radicals formed can undergo (i) addition to  $O_2$ , (ii) abstraction of an oxygen atom from  $H\dot{O}_2$  or  $R\dot{O}_2$ , and (iii)  $\beta$ -scission. Each of these processes becomes prominent as the temperature first decreases and then rises through the period of the delay. Initially, when the temperature is decreasing, there is a buildup of alkylperoxyl radicals, but as the temperature rises, each of these radicals converts back to an alkyl radical and  $O_2$ , where it is consumed by a combination of  $\beta$ -scission and reaction with  $H\dot{O}_2$  and  $R\dot{O}_2$  to form an alkoxy radical and  $\dot{O}H$  or  $R\dot{O}$  radicals.

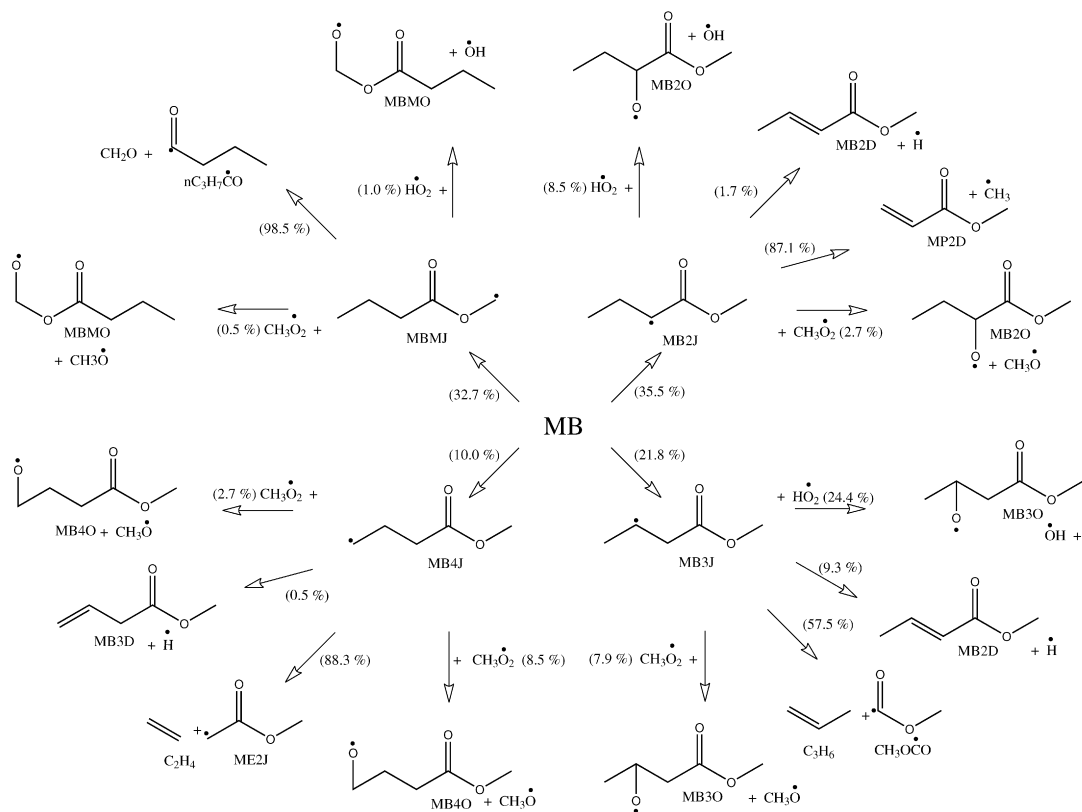


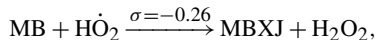
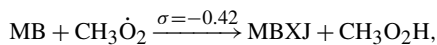
Fig. 14. Chemistry occurring at the point of 50% fuel consumption for 3.13% MB,  $\phi = 0.5$  in Ar at 20 atm and 836 K in a RCM.

The dominant oxygen atom abstraction processes involve the conversion of a  $\text{HO}_2^\bullet$  radical to an  $\text{OH}^\bullet$  radical, which is consumed by reaction with MB. The  $\text{HO}_2^\bullet$  radical is the most abundant radical under RCM conditions (Fig. 15), predominantly formed by the reactions  $\text{HCO} + \text{O}_2 \rightarrow \text{HO}_2^\bullet + \text{CO}$  and  $\text{CH}_3\text{O}^\bullet + \text{O}_2 \rightarrow \text{HO}_2^\bullet + \text{CH}_2\text{O}$ . A sensitivity coefficient of +0.29 shows the importance of the chain-terminating reaction  $\text{HO}_2^\bullet + \text{HO}_2^\bullet \rightarrow \text{H}_2\text{O}_2 + \text{O}_2$ , Fig. 11.

This reaction competes for  $\text{HO}_2$  with hydrogen abstraction from the fuel to form an alkyl radical and  $\text{H}_2\text{O}_2$  ( $\sigma = -0.26$ ), and the abstraction of an O atom from  $\text{HO}_2$  by a fuel alkyl radical to form an alkoxy radical and a reactive  $\dot{\text{O}}\text{H}$  radical ( $\sigma = -0.26$ ), Fig. 12, which further consumes fuel by hydrogen abstraction. The extent to which these alternative  $\text{HO}_2$  consumption channels compete with the chain-terminating reaction has a large influence on the overall reactivity.

Although the concentration of  $\text{CH}_3\dot{\text{O}}_2$  radical is not as high as that of  $\text{H}\dot{\text{O}}_2$  radical, Fig. 15, sensitivity analysis shows that reactions involving this moiety are important. Since  $\text{CH}_3\dot{\text{O}}_2$  radicals do not have a termination channel that is significantly sensitive, sensitivity coefficients of reactions involving this

species and of those involving fuel alkyl radicals can be explained by a consideration of how their reaction compete with reactions involving  $\text{HO}_2$  and the products formed.



where the notation “MBXJ” represents the four primary fuel alkyl radicals that are formed by hydrogen abstraction from MB.

The formation of hydrogen peroxide by hydrogen abstraction from MB shows a lesser sensitivity than the formation of the less stable  $\text{CH}_3\text{O}_2\text{H}$  by the same process, Fig. 12.

This feature is due to the decomposition of  $\text{CH}_3\text{O}_2\text{H}$  to  $\text{CH}_3\dot{\text{O}} + \dot{\text{O}}\text{H}$ . This reaction provides the exothermicity necessary to increase the temperature of the system to cause hydrogen peroxide to decompose, producing a large quantity of  $\dot{\text{O}}\text{H}$  radicals that lead to the ignition event, Fig. 15.

The importance, in a particular system, of the reactions that lead to the  $\text{H}_2\text{O}_2$  decomposition temperature has previously been outlined by Westbrook [55]. Analysis of the reactions responsible for the increase

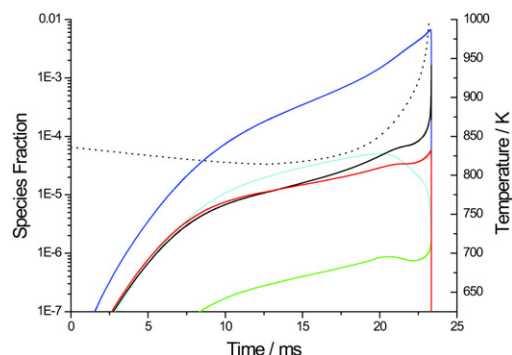
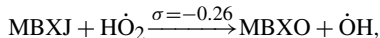
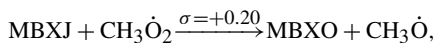


Fig. 15. Predicted species evolution in a RCM for 3.13% MB,  $\phi = 0.5$  in Ar at 836 K and 20 atm. ... Temperature, —  $\text{H}_2\text{O}_2$ , —  $\text{CH}_3\text{O}_2\text{H}$ , —  $\text{CH}_3\text{O}_2^\bullet$ , —  $\text{HO}_2^\bullet$ , — fuel alkyl radicals (MBXJ).

in the temperature of the MB system leading to ignition confirm the involvement of  $\text{CH}_3\text{O}_2\text{H}$  decomposition. At a time of 22.5 ms the reactions contributing to temperature are shown in Chart 13.

Similarly the dichotomy of the reactions



where the notation “MBXO” represents the four alkoxy radicals formed by oxygen atom abstraction from  $\text{HO}_2^\bullet/\text{RO}_2^\bullet$  by each of the four fuel alkyl radicals (Chart 14) can be accounted for by an appreciation of the relative concentrations of the respective species.

The fate of  $\text{HO}_2^\bullet$  controls the reactivity of the system because it is present in abundance, Fig. 15. There

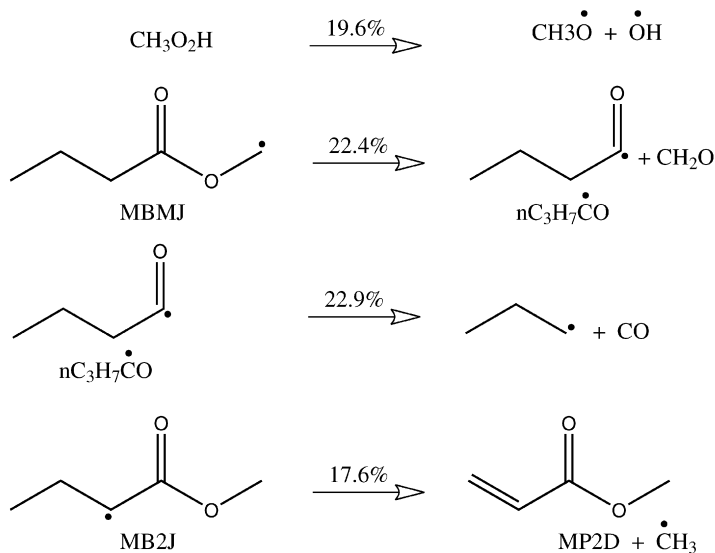


Chart 13.

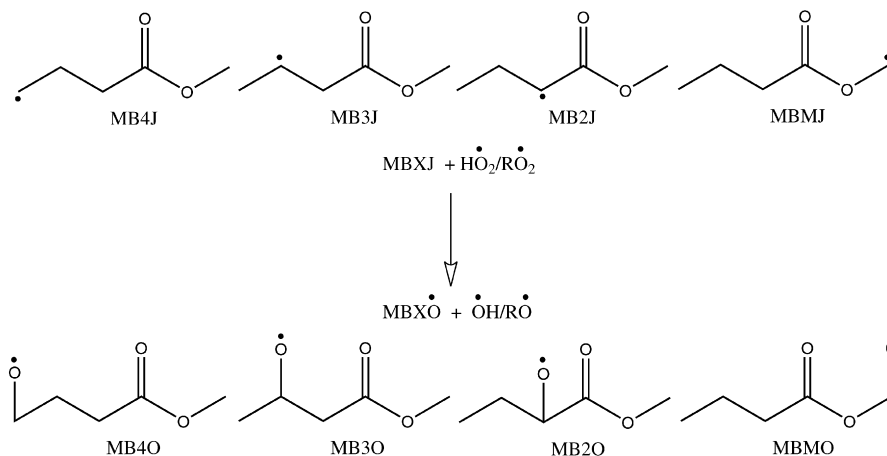


Chart 14.

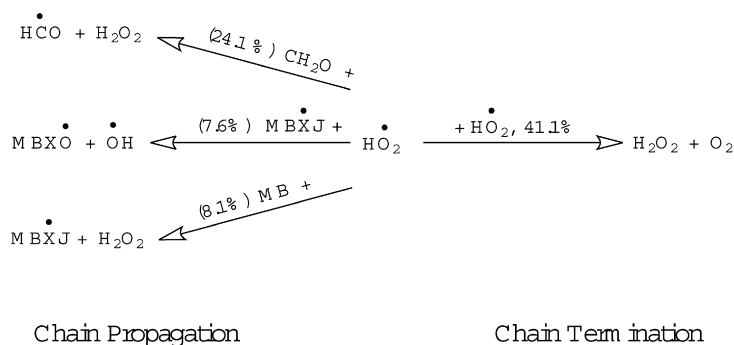


Chart 15.

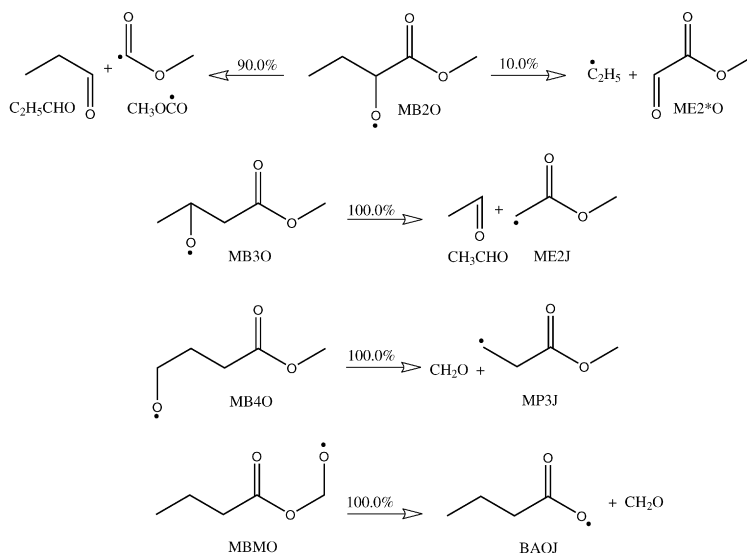


Chart 16.

are a number of competitive channels for its consumption. Broadly speaking these fall into two categories, radical chain propagation and radical chain termination (Chart 15).

The concentration of  $\text{CH}_3\dot{\text{O}}_2$  is high enough, Fig. 15, to allow the consumption of this species to compete with the consumption of  $\text{H}\dot{\text{O}}_2$  radicals.

For every  $\text{CH}_3\dot{\text{O}}_2$  radical consumed by reaction with a fuel alkyl radical, two  $\text{H}\dot{\text{O}}_2$  radicals recombine, slowing the reactivity of the system. For this reason abstraction of an oxygen atom by a fuel alkyl radical from  $\text{H}\dot{\text{O}}_2$  has a negative sensitivity and abstraction of an oxygen atom from  $\text{CH}_3\dot{\text{O}}_2$  has a positive sensitivity.

The inclusion of the reaction of  $\dot{\text{R}} + \text{O}_2 \rightarrow \dot{\text{R}}\text{O}_2$  ( $\sigma = -1$ ) allows more  $\text{H}\dot{\text{O}}_2$  to be consumed by the reaction  $\text{H}\dot{\text{O}}_2 + \text{H}\dot{\text{O}}_2 \rightarrow \text{H}_2\text{O}_2$ , as consequently there is less alkyl radical available to take part in the propagation reaction. Thus, this decreases the reactivity of the system.

Under these conditions of analysis, fuel alkyl radicals are predominantly consumed by decomposition reactions. However, oxygen atom abstraction from  $\text{H}\dot{\text{O}}_2/\text{R}\dot{\text{O}}_2$  is competitive, Fig. 14.

In the case of  $\text{MB2J}$  consumption, oxygen atom abstraction accounts for 10.2% of total consumption, with the formation of  $\text{MP2D}$  the dominant pathway. At 982.4 K,  $\text{MB3J}$  decomposition is almost a factor of 2 slower than  $\text{MB2J}$  decomposition; this allows oxygen atom abstraction to account for a larger portion (32.3%) of  $\text{MB3J}$  consumption relative to  $\text{MB2J}$  consumption.

Generally the formation of a keto ester entity is not favored, but in the case of the  $\text{MB2O}$  alkoxy radical, the keto ester is predicted to be formed in substantial quantities (see Chart 16).

### 5.3. Flow reactor

Marchese et al. [11] have studied the oxidation of methyl butanoate in a flow reactor at a pressure of

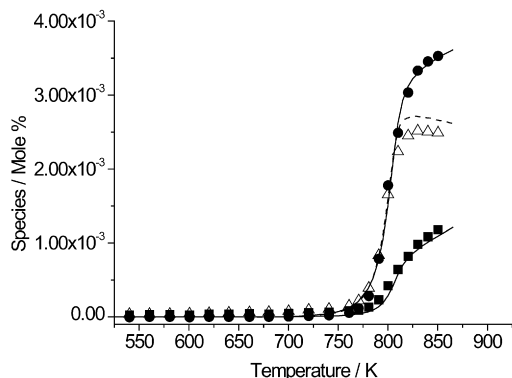


Fig. 16. Flow reactor data [11], 800 ppm MB,  $\phi = 0.35$ , 12.5 atm,  $\tau = 1.8$  s:  $\text{H}_2\text{O}$  ● —,  $\text{CO}$  △ ---,  $\text{CO}_2$  ■ —.

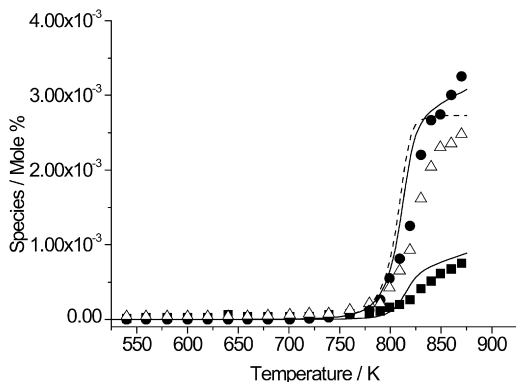


Fig. 18. Flow reactor data [11], 800 ppm MB,  $\phi = 1.0$ , 12.5 atm,  $\tau = 1.8$  s:  $\text{H}_2\text{O}$  ● —,  $\text{CO}$  △ ---,  $\text{CO}_2$  ■ —.

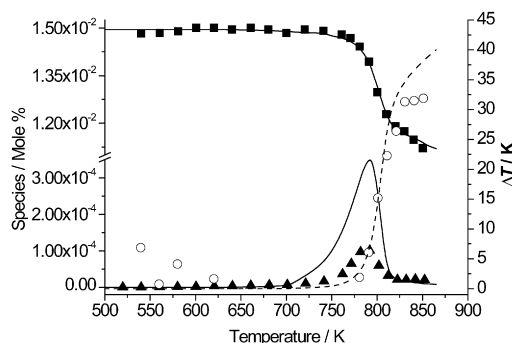


Fig. 17. Flow reactor data [11], 800 ppm MB,  $\phi = 0.35$ , 12.5 atm,  $\tau = 1.8$  s:  $\text{CH}_2\text{O}$  ▲ —,  $\text{O}_2$  ■ —,  $\Delta T$  ○ ---.

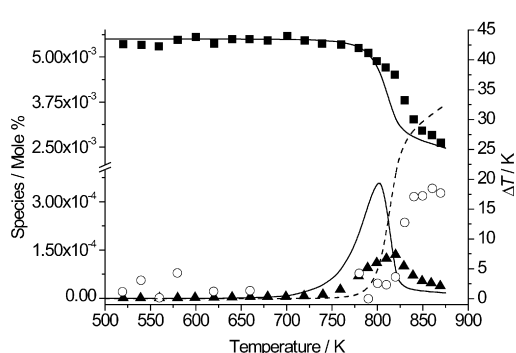


Fig. 19. Flow reactor data [11], 800 ppm MB,  $\phi = 1.0$ , 12.5 atm,  $\tau = 1.8$  s:  $\text{CH}_2\text{O}$  ▲ —,  $\text{O}_2$  ■ —,  $\Delta T$  ○ ---.

12.5 atm, in the temperature range 500–900 K, using 800 ppm MB at equivalence ratios of 0.35, 1.0, and 1.5. They measured changes in temperature ( $\Delta T$ ) and mole fractions of carbon monoxide (CO), carbon dioxide ( $\text{CO}_2$ ), water ( $\text{H}_2\text{O}$ ), oxygen ( $\text{O}_2$ ), and formaldehyde ( $\text{CH}_2\text{O}$ ) as a function of initial reactor temperature at a residence time of 1.8 s. It was observed that increasing the oxygen fraction increased the amounts of CO,  $\text{CO}_2$ , and  $\text{H}_2\text{O}$  produced and shifted the reactivity to lower temperatures. No NTC behavior was observed.

Figs. 16–21 compare experiments (symbols) to model predictions (lines). In general the model reproduces the experimental observations well. However, it does overpredict the concentration of formaldehyde for all conditions. Moreover, under fuel-rich conditions, modeling simulations predict a higher reactivity than is observed experimentally.

At a residence time of 1.8 s in a simulation of the  $\phi = 0.35$  mixture at 780 K, corresponding to 42.5% of MB consumed, analysis reveals that the processes depleting the fuel are hydrogen abstraction by the  $\dot{\text{O}}\text{H}$  (81.7%),  $\text{HO}_2$  (8.8%),  $\dot{\text{H}}$  (8.0%), and  $\text{CH}_3\dot{\text{O}}_2$  (1.5%) radicals (Chart 17). At the temperatures experienced

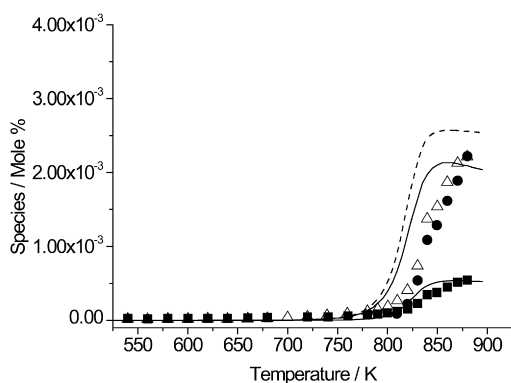


Fig. 20. Flow reactor data [11], 800 ppm MB,  $\phi = 1.5$ , 12.5 atm,  $\tau = 1.8$  s:  $\text{H}_2\text{O}$  ● —,  $\text{CO}$  △ ---,  $\text{CO}_2$  ■ —.

in the flow reactor, the process of abstraction of an oxygen atom from the  $\text{HO}_2/\text{RO}_2$  species is competitive with alkyl radical decomposition.

As in the RCM analysis under similar conditions, MP2D dominates MB2J consumption, with only a minor contribution made by the formation of

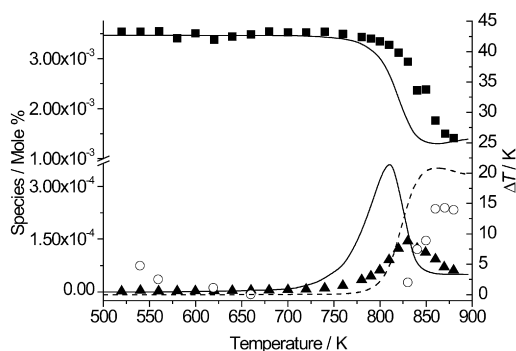
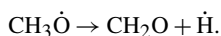
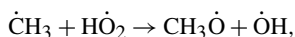
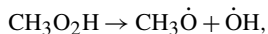


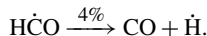
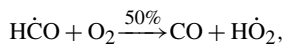
Fig. 21. Flow reactor data [11], 800 ppm MB,  $\phi = 1.5$ , 12.5 atm,  $\tau = 1.8$  s:  $\text{CH}_2\text{O}$   $\blacktriangle$ —,  $\text{O}_2$   $\blacksquare$ —,  $\Delta T$   $\circ$ —.

MB2O (Chart 18). Formaldehyde is most substantially formed via the reaction sequence



$\beta$ -scission of MBMJ is also significant in formaldehyde formation (Chart 19).

Under these conditions, 54% of CO is produced by the consumption of the formyl radical, which is formed by hydrogen abstraction from formaldehyde:



In addition, a further 26.5% of the CO produced is formed by the reaction shown in Chart 20, with  $n\text{C}_3\text{H}_7\dot{\text{C}}\text{O}$  being formed exclusively by MBMJ decomposition.

Given the intrinsic link between CO formation and formaldehyde production/consumption [56–58], it is difficult to reconcile the overprediction of formaldehyde with the accurate prediction of CO by the kinetic model, without considering that formaldehyde is usually difficult to quantify experimentally, as it readily polymerizes to form a nonvolatile solid under ambient conditions [59].

For example, the model shows best agreement with experiment under fuel-lean conditions (Figs. 16 and 17) and the peak discrepancy,  $\approx$  a factor of 3, in

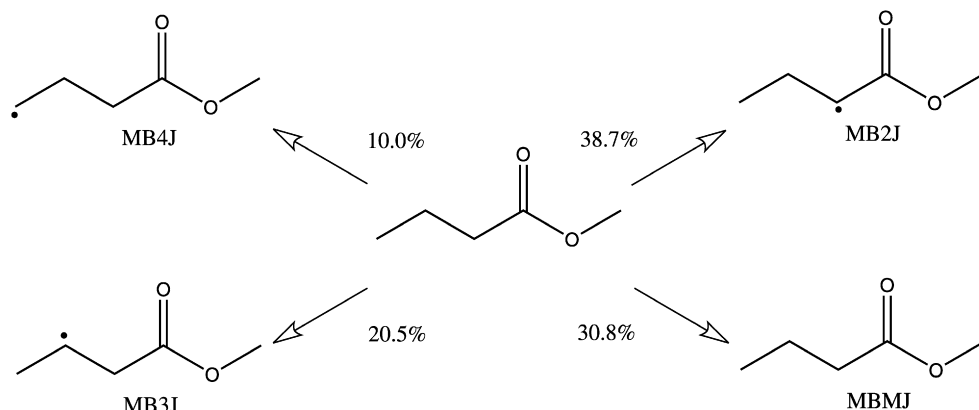


Chart 17.

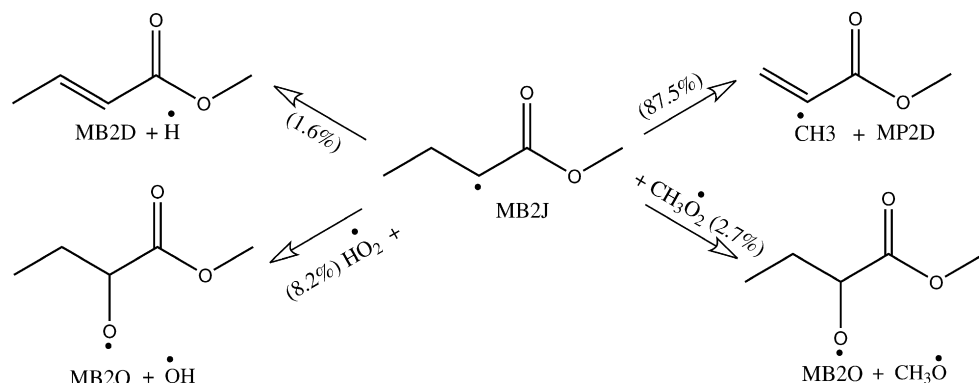


Chart 18.



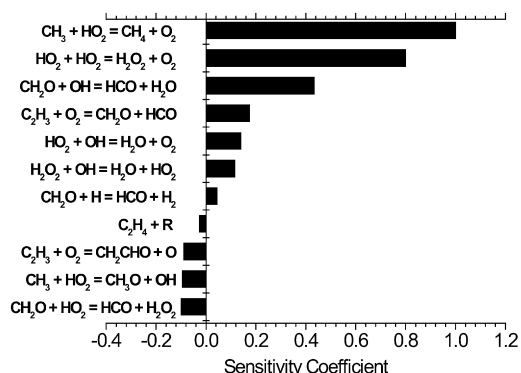
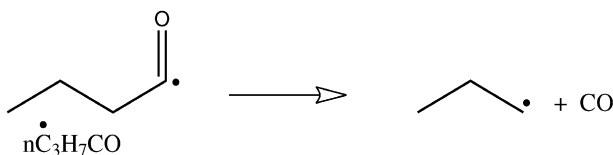
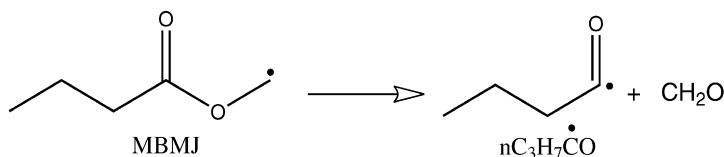


Fig. 22. Sensitivity coefficients for flow reactor conditions for 800 ppm MB,  $\phi = 1.0$  in  $\text{N}_2$  at 820 K and 12.5 atm. [MB] is the sensitive parameter.

the comparison of experimental and simulated  $\text{CH}_2\text{O}$  data is at  $\approx 790$  K. In stark contrast, at this temperature the model predicts the measured CO fraction with precision.

Although the model predictions for the other two conditions occur at slightly cooler temperatures than observed in experiments, the same trend in the over-prediction of peak  $\text{CH}_2\text{O}$  fraction is repeated.

A sensitivity analysis was performed at  $\phi = 1.0$  and 820 K (Figs. 22 and 23). The fuel fraction remaining at a residence time of 1.8 s was used to define the sensitivity parameter,  $\sigma$ , as  $\sigma = ([\text{MB}]' - [\text{MB}])/[\text{MB}]$ , where  $[\text{MB}]'$  is the calculated MB concentration remaining after 1.8 s using the adjusted rate constant. As before, a negative sensitivity coefficient indicates an increase in reactivity and a positive sensitivity coefficient indicates a decrease in reactivity. Sensitivity coefficients have been normalized to a value of one.

The importance of  $\text{HO}_2$  is again apparent: it is the most abundant radical in the system, and similarly to the RCM analysis, the extent of its involvement in the two prominent chain termination channels has a large

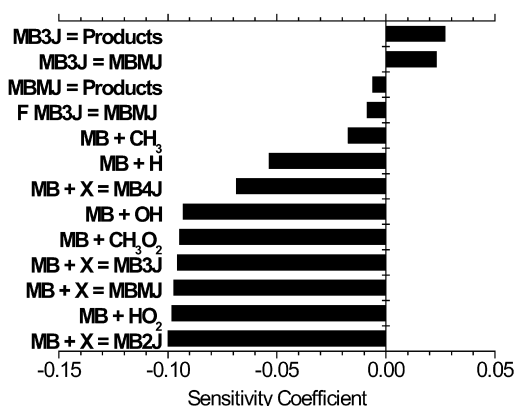
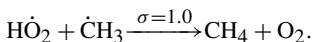
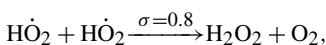
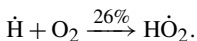
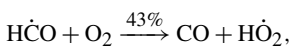


Fig. 23. Sensitivity coefficients for flow reactor conditions for 800 ppm MB,  $\phi = 1.0$  in  $\text{N}_2$  at 820 K and 12.5 atm. [MB] is the sensitive parameter.

influence on the reactivity of the system:



The main reaction accounting for  $\text{HO}_2$  formation in the flow reactor is the reaction of the formyl radical with  $\text{O}_2$ , but unlike the RCM analysis there is a sizeable contribution from the reaction of  $\dot{\text{H}}$  atoms with  $\text{O}_2$ :



Although  $\text{HO}_2$  is the most abundant radical in the system, it is reaction with the more reactive  $\dot{\text{O}}\text{H}$  radical that consumes most of the fuel.

However, the reaction of  $\dot{\text{O}}\text{H}$  with MB is the only reaction involving  $\dot{\text{O}}\text{H}$  that is significantly sensitive, and this reaction has a similar sensitivity coefficient

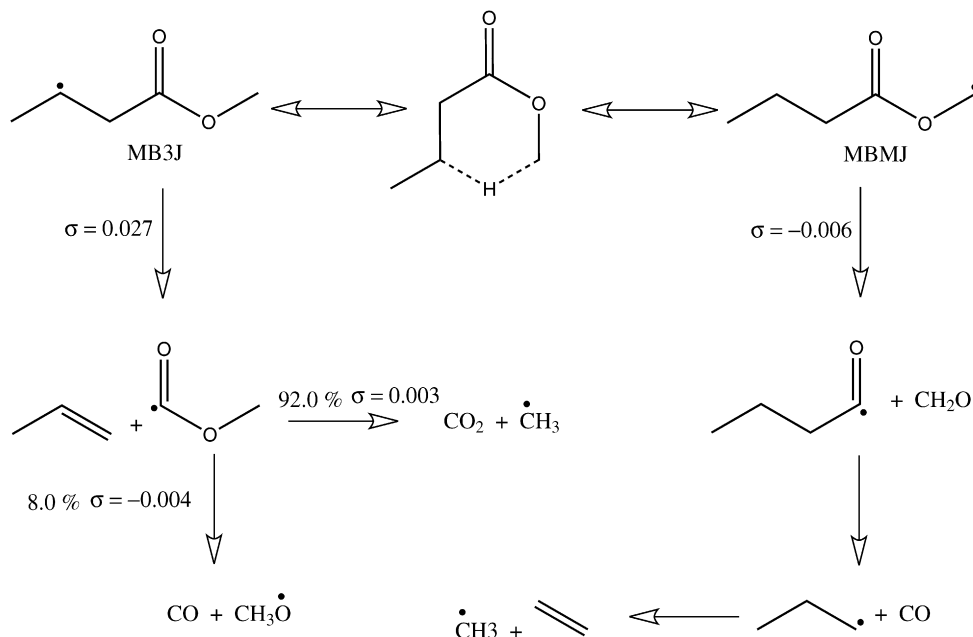
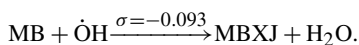
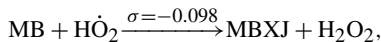
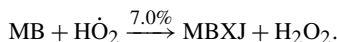
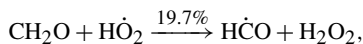
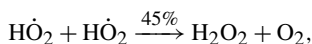


Chart 21.

to the less active reaction of MB with  $\dot{\text{H}}\text{O}_2$ :



This attribute can be explained by examination of the fate of  $\text{H}_2\text{O}_2$ . At these conditions, 72% of  $\dot{\text{H}}\text{O}_2$  is converted to  $\text{H}_2\text{O}_2$  by



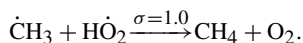
$\text{H}_2\text{O}_2$  subsequently decomposes in a process which accounts for almost half of all  $\dot{\text{O}}\text{H}$  radicals being produced:  $\text{H}_2\text{O}_2 \xrightarrow{100\%} \dot{\text{O}}\text{H} + \dot{\text{O}}\text{H}$ .

As can be seen above, the  $\dot{\text{H}}\text{O}_2$  radical is converted to  $\text{H}_2\text{O}_2$  by a combination of recombination (radical chain termination) and by hydrogen abstraction (radical chain propagation), and it is the balance between these processes and not the subsequent decomposition of  $\text{H}_2\text{O}_2$  that is important in terms of the reactivity of the system; this conclusion is supported by the high sensitivity coefficients of reactions of the  $\dot{\text{H}}\text{O}_2$  radical, Figs. 22 and 23.

Another significant process in the flow reactor simulation is the six-centered isomerization channel interconverting fuel alkyl radicals between the “3” and the “M” positions. The decomposition of these respective radicals have differing influences on the

overall reactivity of the system; MB3J decomposition slows the reactivity of the system, and as the decomposition pathway of MBMJ is more exothermic, it raises the temperature of the system, increasing the overall rate of reaction. MB3J decomposition results in the formation of propene and  $\text{CH}_3\text{O}\dot{\text{C}}\text{O}$ , whereas MBMJ decomposition results in the production of formaldehyde and eventually the *n*-propyl radical and carbon monoxide (Chart 21).

The decomposition of the  $\text{CH}_3\text{O}\dot{\text{C}}\text{O}$  radical has been the subject of recent attention [60,61]. We use the expression of Glaude et al. [60], who performed calculations on  $\text{CH}_3\text{O}\dot{\text{C}}\text{O}$  decomposition using the CBS-Q method. Glaude et al. applied their result in a modeling study of dimethyl carbonate oxidation against speciation data collected in an opposed-flow diffusion flame with good agreement to experiment attained. The decomposition of  $\text{CH}_3\text{O}\dot{\text{C}}\text{O}$  is important, as the model predicts that the majority forms  $\text{CO}_2$  and the  $\dot{\text{C}}\text{H}_3$  radical, with methyl production leading to  $\dot{\text{H}}\text{O}_2$  chain termination in the most sensitive reaction in the system:



Under fuel-rich conditions, the competition between isomerization and  $\beta$ -scission of the MBMJ radical becomes important, as the net rate of isomerization favors the formation of MB3J.

MBMJ consumption occurs by a series of exothermic  $\beta$ -scission reactions, which are substantially responsible for raising the temperature of the system

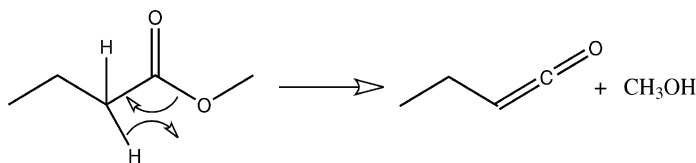


Chart 22.

and “driving” the reactivity. If MBMJ decomposition cannot compete to a sufficient extent with the isomerization pathway, a downturn in reactivity results as temperature increases. Particular attention to this decomposition rate expression was required to prevent such a downturn in reactivity, which was not seen in experiments.

#### 5.4. Jet-stirred reactor

Figs. 25–28 compare model simulations (lines) with the jet-stirred reactor data of Gail et al. [12] (symbols). In general, simulations are in good qualitative and quantitative agreement. However, with the exception of propyne ( $p\text{-C}_3\text{H}_4$ ), in instances where species are measured at low abundance, the quantitative agreement is very poor, Fig. 26. Although we have not included the data here, the model has also been tested against the JSR data of Sarathy et al. [13] and shows roughly the same level of agreement, unsurprisingly so, as the experimental conditions are very similar.

In contrast to the flame environment, the experimentally observed fuel profile is not well predicted by the model, but the formaldehyde data are. We feel it necessary to qualify the simulations in this section, as the JSR experiments of Gail et al. and those of Sarathy et al. both show that high levels of methanol and other oxygenates are formed during MB oxidation at relatively low temperatures (800–1000 K). In stark contrast, the model predicts that methanol will be formed in minute quantities at these temperatures. We have not been able to modify the model in any meaningful way to account for the high methanol concentration. Nor have we been able to improve agreement with the fuel data without compromising agreement with shock tube ignition delays, in addition to the other species measured in both the JSR and flame environments.

Gail et al. and Sarathy et al. offer no explanation for the mechanism of methanol formation from MB. However, El-Nahas et al. [17] have used CBS-QB3 methods and transition state theory to calculate an activation energy of  $74.8 \text{ kcal mol}^{-1}$  for the formation of methanol and butanal from MB by a unimolecular elimination reaction (see Chart 22).

Clearly this high energy barrier cannot account for methanol production under the conditions stud-

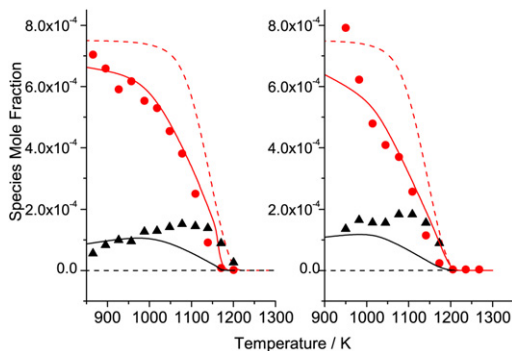


Fig. 24. Jet-stirred reactor data of Sarathy et al. (left) and Gail et al. (right). ● MB, ▲  $\text{CH}_3\text{OH}$ , --- unmodified model, - - - inclusion of wall-catalyzed elimination. (For interpretation of the references to color in this figure legend, the reader is referred to the web version of this article.)

ied. However, examination of the methanol profiles under both conditions shows that there is very little increase in the rate of production of methanol with increase in temperature, behavior consistent with a low-activation-energy process.

It has previously been established [63–66] that the study of oxygenated fuels in this type of reactor can be complicated by heterogeneous catalysis by Si–OH sites on the reactor wall, resulting in the molecular decomposition of fuel.

If the assumption is made that MB decomposes to methanol and butanal with a rate constant of  $20 \exp(-4000 \text{ cal mol}^{-1}/RT) \text{ cm}^3 \text{ mol}^{-1} \text{ s}^{-1}$ , the observed methanol and MB profiles of Gail et al. and those of Sarathy et al. can be simulated with much improved accuracy, and crucially without severe loss of agreement elsewhere, Fig. 24. For the purpose of validating the kinetic model proposed in this study, we compensate for the above process (assuming it is occurring) by using the measured species fraction at 950 K as the initial condition. The calculated carbon balances of 108.1 and 92% allowing for this adjustment to the stated initial conditions of Gail et al. and Sarathy et al. are still well within the error of  $100 \pm 10\%$  and  $100 \pm 15\%$  reported by the respective authors.

The model can successfully reproduce most data with this adjustment to the initial conditions. An exception is in the case of trace species, Fig. 26, where

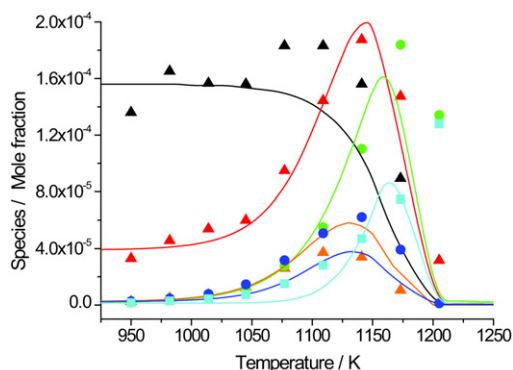


Fig. 25. Jet-stirred reactor data [12], 0.075% MB,  $\phi = 1.13$ , 1.0 atm,  $\tau = 0.07$  s:  $C_3H_6$  ●, MP2D ▲,  $CH_4$  ●,  $CH_3OH$  ▲,  $C_2H_2$  ■, and  $CH_2O$  ▲. (For interpretation of the references to color in this figure legend, the reader is referred to the web version of this article.)

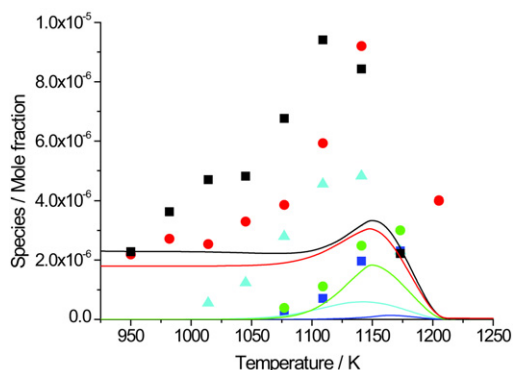


Fig. 26. Jet-stirred reactor data [12], 0.075% MB,  $\phi = 1.13$ , 1.0 atm,  $\tau = 0.07$  s:  $CH_3CHO$  ●,  $1-C_4H_8$  ▲,  $p-C_3H_4$  ●, Acrolein ■, and  $C_4H_6$  ■. (For interpretation of the references to color in this figure legend, the reader is referred to the web version of this article.)

only propyne ( $p-C_3H_4$ ) is well predicted. The remaining species are oxygenates and  $C_4$  intermediates. There exists no direct route to the formation of 1-butene or butadiene from MB other than the recombination of radicals during the quench, a process that is not easily simulated and not performed in this study. We would further postulate that the presence of the oxygenates may be distorted by the proposed wall catalysis of fuel and thus difficult to simulate successfully.

Analysis of the chemistry occurring inside the JSR at 1150 K at a residence time of 70 ms reveals that hydrogen abstraction by  $\dot{H}$  atoms accounts for 61.7% of fuel consumed, with hydrogen abstraction by  $\dot{OH}$ ,  $\dot{CH}_3$  radicals, and O atoms accounting for 17.4, 2.9, and 5.1%, respectively. Due to the relatively high temperatures in the JSR, the remaining 12.9% of MB

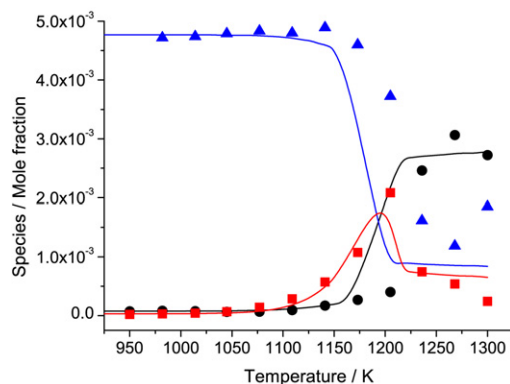


Fig. 27. Jet-stirred reactor data [12], 0.075% MB,  $\phi = 1.13$ , 1.0 atm,  $\tau = 0.07$  s:  $O_2$  ▲, CO ■, and  $CO_2$  ●. (For interpretation of the references to color in this figure legend, the reader is referred to the web version of this article.)

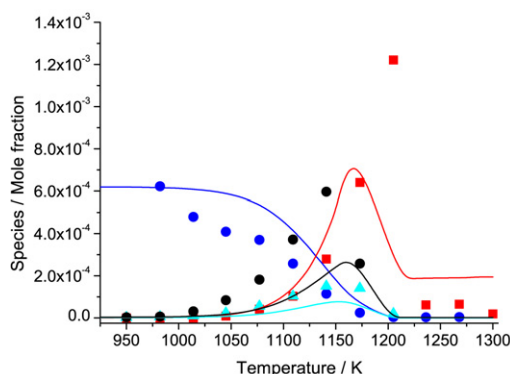


Fig. 28. Jet-stirred reactor data [12], 0.075% MB,  $\phi = 1.13$ , 1.0 atm,  $\tau = 0.07$  s: MB ●,  $H_2$  ■,  $C_2H_6$  ▲, and  $C_2H_4$  ●. (For interpretation of the references to color in this figure legend, the reader is referred to the web version of this article.)

consumption is via unimolecular fuel decomposition (see Chart 23).

Among the major species measured were hydrogen (Fig. 28), with a peak concentration at 1200 K, and ethene (Fig. 28) and propene (Fig. 25), which peak at 1140 K. The model shows that propene is being formed in significant quantities via two pathways:

- (1) the decomposition of MB3J (50%);
- (2) the decomposition of the  $n$ -propyl radical (15%), which is formed by the eventual decomposition of MBMJ via  $nC_3H_7\dot{C}O$ .

The  $n$ -propyl radical plays a more significant role in the formation of  $C_2H_4$ , however, accounting for 50% of the total (Chart 24).

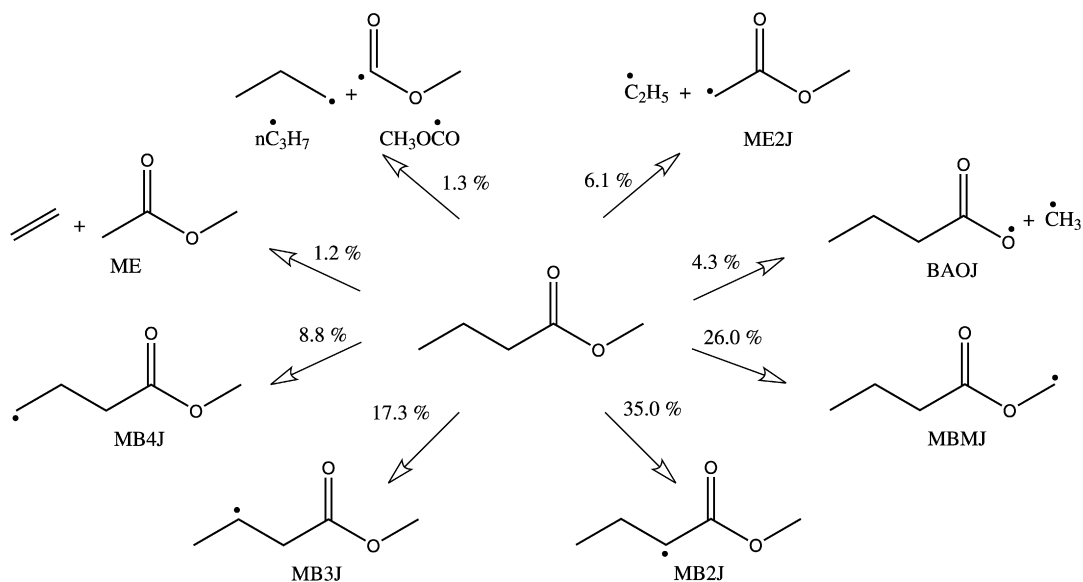


Chart 23.

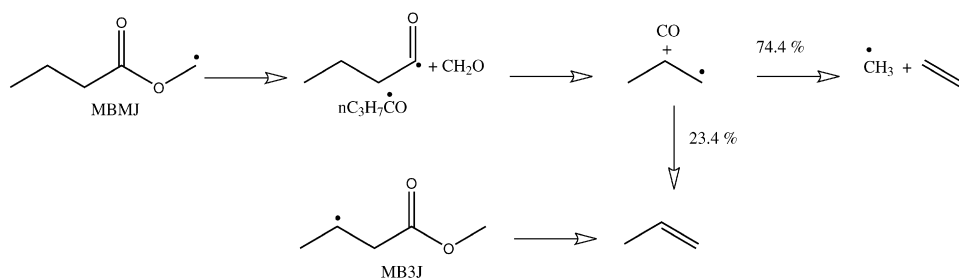


Chart 24.

The remaining  $C_2H_4$  is formed by decomposition of the ethyl radical and unimolecular fuel decomposition. It should be noted that unimolecular fuel decomposition also plays an important role in the formation of the ethyl radical. Methane formation is via hydrogen abstraction from formaldehyde by  $\dot{C}H_3$  radicals, while abstraction by  $\dot{C}H_3$  radicals from  $H_2$  and  $\dot{C}H_3$  radical reactions with  $HO_2$  also contribute to methane formation.

Hydrogen abstraction by  $\dot{H}$  atoms accounts for the formation of  $H_2$ , with abstraction from the fuel (44%) and from formaldehyde (26%) the most significant processes.

A sensitivity analysis was performed under these conditions using the fuel fraction as the sensitivity parameter, with the sensitivity coefficient generated in the same manner as the flow reactor section, Fig. 29. The importance of the chain-branching reaction  $\dot{H} + O_2 \rightarrow \dot{O} + \dot{O}H$  is obvious.

Any reaction that competes with this process for  $\dot{H}$  atom shows a positive sensitivity coefficient, indicating a slowing of the overall reactivity. This effect

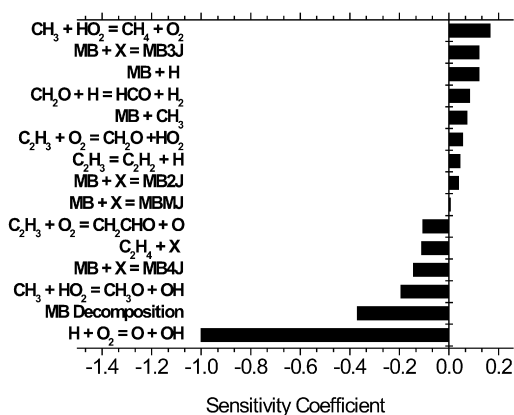
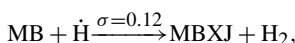
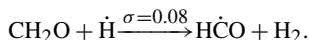


Fig. 29. Sensitivity coefficients for jet-stirred reactor conditions for 0.075% MB,  $\phi = 1.13$  in  $N_2$  at 1150 K, 1 atm, and  $\tau = 0.07$  s. [MB] is the sensitive parameter.

is exhibited in the reactions





The sensitivity coefficients for hydrogen abstraction from the fuel are positive regardless of the site of abstraction (Fig. 29), since abstraction by  $\dot{\text{H}}$  atoms is the dominant process. However, as in the shock tube, and for the same reasons, the exception to this trend is in the case of abstraction from the terminal position on the MB alkyl chain producing MB4J, which shows a large negative sensitivity (Fig. 29). The transition from intermediate to high-temperature chemistry in the JSR allows unimolecular fuel decomposition to become significant. Increasing the rate constant of this reaction class increases the overall rate of reaction (Fig. 29) due to the production of two reactive radicals from one fuel molecule, again similarly to the shock tube study.

### 5.5. Opposed-flow diffusion flame

Gail et al. [12] also studied MB oxidation in an opposed-flow diffusion flame. A stream of 4.7% MB diluted in  $\text{N}_2$  was sent through the bottom burner port, while the oxidizer stream, containing 42%  $\text{O}_2$ , also diluted in  $\text{N}_2$ , was sent through the top burner port. The authors report that the fuel and oxidizer streams meet in a well-defined stagnation point flow [67]. Speciation measurements as a function of distance from the fuel port (effectively temperature) were performed. These data provide the only other quantification of MB in a reactive environment, the other major species measured were carbon monoxide (CO), carbon dioxide ( $\text{CO}_2$ ), ethane ( $\text{C}_2\text{H}_6$ ), propene ( $\text{C}_3\text{H}_6$ ), ethene ( $\text{C}_2\text{H}_4$ ), ethyne ( $\text{C}_2\text{H}_2$ ), and methane ( $\text{CH}_4$ ), including formaldehyde ( $\text{CH}_2\text{O}$ ), propane ( $\text{C}_3\text{H}_8$ ), propyne ( $p\text{-C}_3\text{H}_4$ ), ethanal ( $\text{CH}_3\text{CHO}$ ), 1-butene (1- $\text{C}_4\text{H}_8$ ), and butadiene ( $\text{C}_4\text{H}_6$ ) formed in smaller quantities. Species measurements were taken in the region of 2–8 mm from the fuel port, corresponding to a temperature range of 355–1560 K.

Simulations performed both by (i) solving the gas energy equation to compute the temperature profile and by (ii) by using the experimentally measured temperature profile were very similar.

Figs. 30–34 depict the data of Gail et al. [12] (symbols) with the simulations (lines) generated using the experimental temperature profile. The model proves satisfactorily accurate in predicting the profiles of MB, CO,  $\text{CO}_2$ ,  $\text{C}_2\text{H}_4$ ,  $\text{C}_2\text{H}_6$ , and  $\text{C}_3\text{H}_6$ . With the exception of the CO fraction, there is qualitative agreement with all profiles, in that the simulated position of the peak species fraction is well predicted by the model. What is not satisfactory is the overprediction by a factor of between 2 and 3 of  $\text{C}_2\text{H}_2$ ,  $\text{CH}_4$ , and  $p\text{-C}_3\text{H}_4$  and the underprediction to roughly the same degree of  $\text{C}_3\text{H}_8$ ,  $\text{C}_4\text{H}_6$ , 1- $\text{C}_4\text{H}_8$ , and  $\text{CH}_3\text{CHO}$ ,

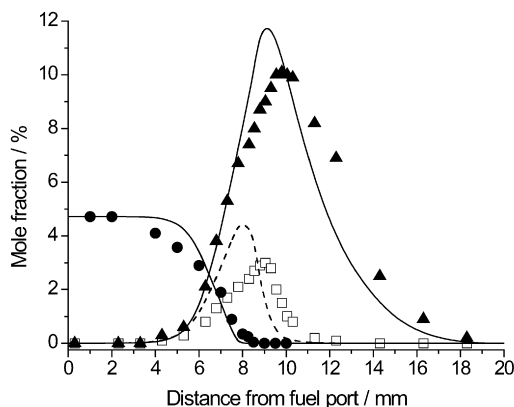


Fig. 30. Opposed-flow diffusion flame data [12]. MB ● —,  $\text{CO}_2$  ▲ —, and CO □ ---.

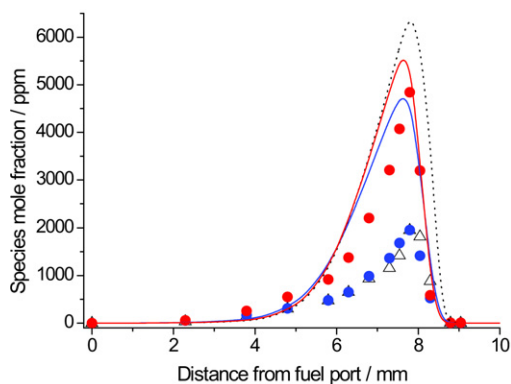


Fig. 31. Opposed-flow diffusion flame data [12].  $\text{C}_2\text{H}_4$  ● —,  $\text{C}_2\text{H}_2$  ▲ —, and  $\text{CH}_4$  ● —. (For interpretation of the references to color in this figure legend, the reader is referred to the web version of this article.)

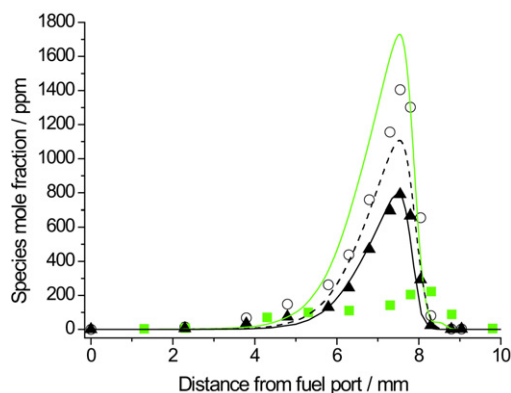


Fig. 32. Opposed-flow diffusion flame data [12].  $\text{C}_2\text{H}_6$  ○ ---,  $\text{C}_3\text{H}_6$  ▲ —, and  $\text{CH}_2\text{O}$  ■ —. (For interpretation of the references to color in this figure legend, the reader is referred to the web version of this article.)



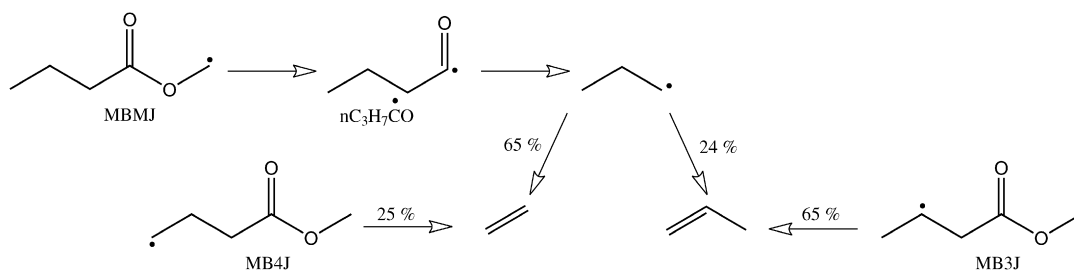


Chart 25.

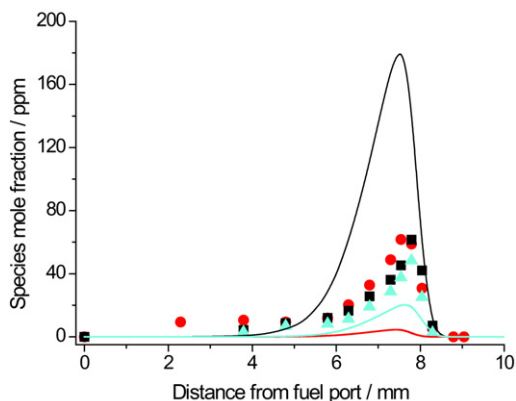


Fig. 33. Opposed-flow diffusion flame data [12].  $\text{C}_3\text{H}_8$  ● —, butadiene ▲ —, and  $p\text{-C}_3\text{H}_4$  ■ —. (For interpretation of the references to color in this figure legend, the reader is referred to the web version of this article.)

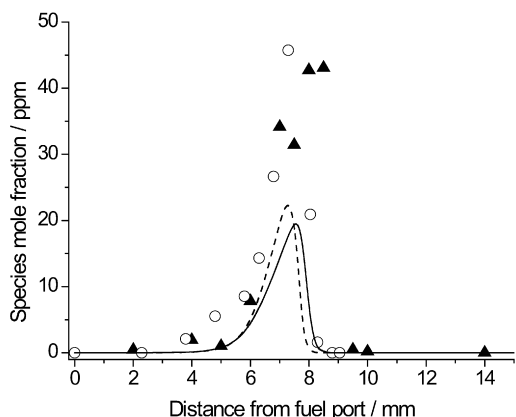


Fig. 34. Opposed-flow diffusion flame data [12].  $1\text{-C}_4\text{H}_8$  ○ --- and  $\text{CH}_3\text{CHO}$  ▲ —.

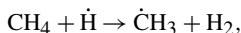
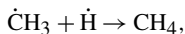
while the simulated  $\text{CH}_2\text{O}$  profile falls into a category all of its own. However, as in the case of the simulated  $\text{CH}_2\text{O}$  profile in the flow reactor environment, it is difficult to rationalize the accurate prediction of CO with this level of disagreement in the prediction of formaldehyde.

Model predictions of ethene and propene are in good agreement with experiment. As in the JSR, the formation of these species is linked by the branching of the decomposition of the  $n\dot{\text{C}}_3\text{H}_7$  (*n*-propyl) radical, and therein to MBMJ decomposition. Decomposition of two of the remaining three fuel alkyl radicals also results in the direct formation of ethene or propene. These reactions are shown in Chart 25, where the percentages refer to the  $\text{C}_2\text{H}_4/\text{C}_3\text{H}_6$  formation and the branching ratio for the decomposition of the  $n\dot{\text{C}}_3\text{H}_7$  radical is 80:20 in favor of  $\text{C}_2\text{H}_4$  formation.

The accurate prediction of these intermediates indicate that the rate constants used for hydrogen abstraction from MB and for fuel alkyl radical decompositions are reasonably accurate.

In contrast,  $\text{C}_2\text{H}_2$  and  $\text{CH}_4$  profiles are overpredicted, while  $\text{C}_2\text{H}_6$  is underpredicted. These species are of importance, as their formation lies along the reaction pathway that is largely responsible for the overall reactivity of the system: the competition between methyl radical recombination to form ethane and recombination with H atom to form methane shown in Chart 26, where the percentages refer to methane formation and methyl consumption.

This attribute can be seen by examination of the high sensitivity coefficients (Fig. 35) associated with the following reactions:



Since the temperatures experienced in the diffusion flame cover intermediate and high temperatures, it is necessary to analyze the chemistry at points representative of both regimes. The sensitivity analysis has been conducted at distances of 6.8 and 7.8 mm from the fuel inlet, corresponding to temperatures of 913 and 1470 K, respectively. Standard Chemkin methods have been used to generate the sensitivity coefficients with the sensitivity parameter again the concentration of MB. Sensitivity coefficients have been normalized to a value of one.

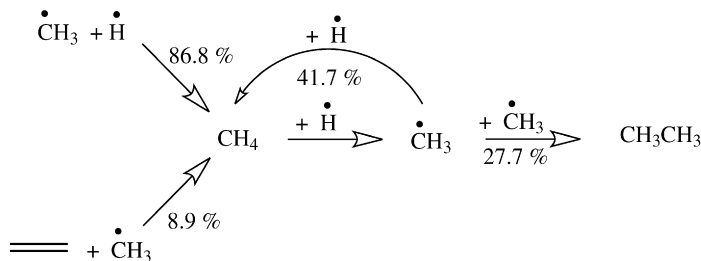


Chart 26.

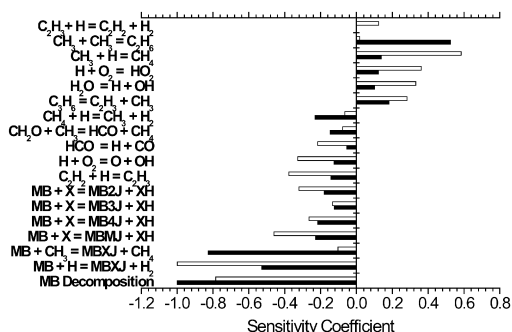


Fig. 35. Sensitivity coefficients of opposed-flow diffusion flame simulations for (black) 6.80 mm from bottom inlet (913 K) and (white) 7.85 mm from bottom inlet (1470 K). [MB] is the sensitive parameter.

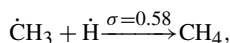
The sensitivity analysis can be explained by consideration of two domains:

### 5.5.1. High temperature

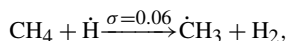
At high temperature (1470 K), 93% of MB is consumed by hydrogen abstraction, with  $\dot{\text{H}}$  atoms (81%) and  $\dot{\text{O}}\text{H}$  radicals (9%) the main contributors, resulting in the flux analysis shown in Chart 27, and under this condition fuel alkyl radicals are consumed by  $\beta$ -scission.

Due to the significant role of  $\dot{\text{H}}$  atoms in fuel consumption, reactions involving this moiety show large sensitivity coefficients (Fig. 35). Hydrogen abstraction from MB by  $\dot{\text{H}}$  atoms is the most sensitive re-

action at 1470 K ( $\sigma = -1$ ); this is so because this process results in the formation of a fuel alkyl radical and  $\text{H}_2$  (i.e., propagation) and is in competition for  $\dot{\text{H}}$  atoms with the chain termination reaction of



which shows a large positive sensitivity, slowing the overall rate of reaction. As this reaction is coupled to the dominant methane consumption reaction,



this reaction pathway leads to the consumption of two reactive  $\dot{\text{H}}$  atoms, and the extent to which it competes for  $\dot{\text{H}}$  atoms with hydrogen abstraction from MB is responsible for the overall reactivity of the system at high temperatures.

### 5.5.2. Intermediate temperature

At 913 K the sensitivity of hydrogen abstraction from MB by  $\dot{\text{H}}$  atom is diminished due to the activity of the  $\dot{\text{C}}\text{H}_3$  radical. At this point in the flame the model shows that 70% of the initial fuel fraction is consumed. Hydrogen abstraction by the  $\dot{\text{C}}\text{H}_3$  radical (47.4%) and  $\dot{\text{H}}$  atom (46.7%) are mainly responsible, with unimolecular fuel decomposition contributing 2.0%. The dual activity of abstraction by the  $\dot{\text{C}}\text{H}_3$  radical and by  $\dot{\text{H}}$  atoms allows the “2” position to be the favored site of abstraction, by an unusually clear margin due to its much lower C–H bond enthalpy (Chart 28).

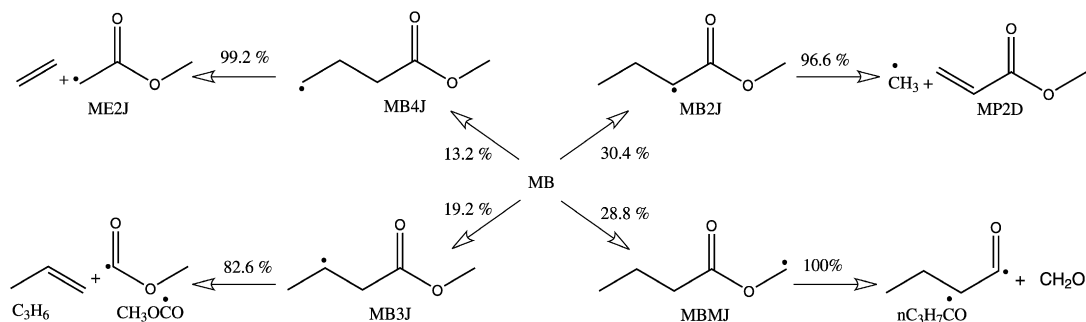


Chart 27.

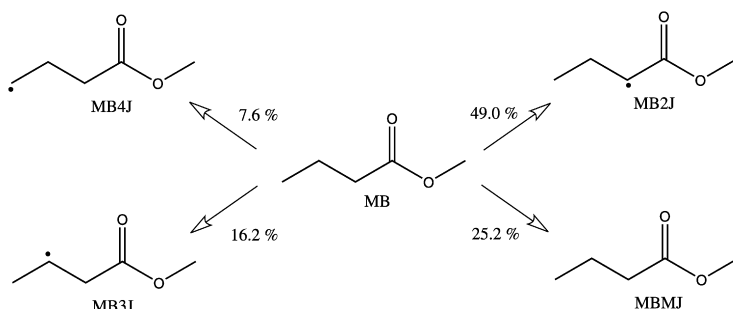


Chart 28.

As intermediate temperatures (800–1000 K) allow hydrogen abstraction by both  $\dot{\text{C}}\text{H}_3$  radicals and  $\dot{\text{H}}$  atoms to consume MB, processes involving the  $\dot{\text{C}}\text{H}_3$  radical play a more significant role at lower temperatures (Fig. 35); therefore, under this condition, reactions involving the  $\dot{\text{C}}\text{H}_3$  radical show larger sensitivity coefficients than where the flame is hotter.

The recombination of methyl radicals to form ethane shows the largest positive sensitivity (Fig. 35), and the activity of this chain-terminating process explains why hydrogen abstraction from MB by  $\dot{\text{C}}\text{H}_3$  radicals shows a much larger sensitivity relative to abstraction by  $\dot{\text{H}}$  atoms (Fig. 35). Even though each process accounts for approximately the same portion of MB consumption, hydrogen abstraction by the  $\dot{\text{C}}\text{H}_3$  radical faces competition from ethane formation, which consumes two methyl radicals.

Over both domains, the branching between  $\dot{\text{C}}\text{H}_3$  radical recombination to form ethane at intermediate temperatures and  $\dot{\text{C}}\text{H}_3$  radical recombination with  $\dot{\text{H}}$  atom to form methane at high temperatures regulates the reactivity of the system.

The agreement with  $\text{C}_2\text{H}_6$  and  $\text{CH}_4$  profiles can be improved by increasing the rate constant of  $\dot{\text{C}}\text{H}_3$  radical recombination to form ethane. However, to do so results in a less reactive system and the activity of other species is not as well represented. It is interesting to note that the prediction of  $\text{C}_2\text{H}_4/\text{C}_2\text{H}_2$  profiles is not affected by changes to the rate constant of methyl recombination. Since  $\text{C}_2\text{H}_2$  is formed by radical attack on  $\text{C}_2\text{H}_4$  via the vinyl radical and  $\text{C}_2\text{H}_4$  is well predicted by the model, we are forced to conclude that the overprediction of  $\text{C}_2\text{H}_2$  is due to an imbalance in the rate constants of vinyl decomposition versus vinyl addition to molecular oxygen. The purpose of this study has been to improve the description of the chemistry responsible for MB oxidation to the point of smaller hydrocarbon and oxygenated hydrocarbon intermediate species. Optimization of the processes responsible for vinyl radical consumption is better suited to more well-understood systems and has not been attempted here.

## 6. Conclusions

This study provides shock tube and rapid compression machine autoignition measurements of a biodiesel surrogate, methyl butanoate. Our results show that methyl butanoate does not exhibit NTC behavior, as has been reported [62] for long-chain methyl esters typical of biodiesel constituents. Therefore, MB is not an ideal surrogate molecule for a detailed study of biodiesel oxidation/combustion. However, it can serve as a starting point for the detailed study of larger methyl esters.

The autoignition data, as well as speciation data reported in the literature, have been used to produce a validated kinetic model over the temperature range 600–1700 K and the pressure range 1–40 atm. Model predictions generally agree well with experiment, indicating that most of the reaction pathways and accompanying reaction rates are described reasonably well. However, this conclusion will only be tested by new experimental data. Analysis of the kinetic model has shown that under each condition of temperature, pressure, and equivalence ratio, different reaction pathways become prominent. In particular, the importance of unimolecular fuel decomposition at high temperatures, the processes of the  $\text{HO}_2$  radical at low to intermediate temperatures, and the importance of fuel alkyl radical decomposition under fuel-rich conditions is highlighted. Additional data and model validation at intermediate temperature and under fuel-rich conditions is required for further optimization of fuel alkyl radical decomposition and isomerization rate constants, leading to more accurate prediction of fuel and primary intermediate species profiles.

## Acknowledgments

Financial support was provided by Science Foundation Ireland under the Research Frontiers Programme (2004/Br/C0146) and by an EU Marie Curie Transfer of Knowledge grant (MKTD-CT-2004-

517248). Thanks to Professor Murray Thompson (University of Toronto, Canada) for the provision of flame data, and also to Professor Joseph Bozzelli (New Jersey Institute of Technology, USA) for insight and discussion in the formulation of a treatment to account for pressure fall-off.

## References

- [1] B. Metz, O.R. Davidson, P.R. Bosch, R. Dave, L.A. Meyer, *Climate Change 2007: Mitigation. Contribution of Working Group III to the Fourth Assessment Report of the Intergovernmental Panel on Climate Change*, IPCC/Cambridge University Press, Cambridge, UK/New York, 2007.
- [2] A.K. Agarwal, *Prog. Energy Combust. Sci.* 33 (2007) 233–271.
- [3] M.S. Graboski, R.L. McCormick, *Prog. Energy Combust. Sci.* 24 (1998) 125–164.
- [4] W.J. Pitz, N.P. Cernansky, F.L. Dryer, F.N. Egolfopoulos, J.T. Farrell, D.G. Friend, H. Pitsch, SAE Paper 2007-01-0175.
- [5] C.V. Naik, W.J. Pitz, M. Sjöberg, J.E. Dec, J. Orme, H.J. Curran, J.M. Simmie, C.K. Westbrook, SAE paper 2005-01-3742.
- [6] E.M. Fisher, W.J. Pitz, H.J. Curran, C.K. Westbrook, *Proc. Combust. Inst.* 28 (2000) 1579–1586.
- [7] B.I. Parsons, C.J. Danby, *J. Chem. Soc.* (1956) 1795–1798.
- [8] B.I. Parsons, C. Hinshelwood, *J. Chem. Soc.* (1956) 1799–1803.
- [9] B.I. Parsons, *J. Chem. Soc.* (1956) 1804–1809.
- [10] D.E. Hoare, T.M. Li, A.D. Walsh, *Proc. Combust. Inst.* 11 (1967) 879–887.
- [11] A.J. Marchese, M. Angioletti, F.L. Dryer, in: *International Symposium on Combustion 2004, Work-in-progress poster IF1-03*.
- [12] S. Gail, M.J. Thomson, S.M. Sarathy, S.A. Syed, P. Dagaut, P. Diévert, A.J. Marchese, F.L. Dryer, *Proc. Combust. Inst.* 31 (2007) 305–311.
- [13] S.M. Sarathy, S. Gail, S.A. Syed, M.J. Thomson, P. Dagaut, *Proc. Combust. Inst.* 31 (2007) 1015–1022.
- [14] W.R. Schwartz, S.E. McEnally, L.D. Pfefferle, *J. Phys. Chem. A* 110 (2006) 6643–6648.
- [15] W.K. Metcalfe, S. Dooley, H.J. Curran, J.M. Simmie, A.M. El-Nahas, M.V. Navarro, *J. Phys. Chem. A* 111 (2007) 4001–4014.
- [16] T. Vaughan, M. Wessel, M. Harris, A.J. Marchese, in: *AIAA Aerospace Sciences Meeting and Exhibit, 2007*, paper 0741.
- [17] A.M. El-Nahas, M.V. Navarro, J.M. Simmie, J.W. Bozzelli, H.J. Curran, S. Dooley, W. Metcalfe, *J. Phys. Chem. A* 111 (2007) 3727–3739.
- [18] C.K. Westbrook, W.J. Pitz, H.J. Curran, *J. Phys. Chem. A* 110 (2006) 6912–6922.
- [19] J.M. Smith, Ph.D. thesis, National University of Ireland, Galway, 2004.
- [20] J.M. Smith, J.M. Simmie, H.J. Curran, *Int. J. Chem. Kinet.* 37 (2005) 728–736.
- [21] D.C. Horning, D.F. Davidson, R.K. Hanson, in: *23rd Int. Symp. Shock Waves*, 2001, paper 5732.
- [22] A. Lifshitz, in: G. Ben-Dor, O. Igra, T. Elperin (Eds.), *Handbook of Shock Waves*, vol. 3, Academic Press, San Diego, 2001, pp. 212–256.
- [23] C. Morley, <http://www.gaseq.co.uk/>.
- [24] L. Brett, J. MacNamara, P. Musch, J.M. Simmie, *Combust. Flame* 124 (2001) 326–329.
- [25] E.J. Silke, H.J. Curran, J.M. Simmie, *Proc. Combust. Inst.* 30 (2005) 2639–2647.
- [26] D. Lee, S. Hochgreb, *Combust. Flame* 114 (1998) 531–545.
- [27] J. Würmel, J.M. Simmie, *Combust. Flame* 141 (2005) 417–430.
- [28] D. Lee, Ph.D. thesis, Massachusetts Institute of Technology, 1997.
- [29] H.J. Curran, P. Gaffuri, W.J. Pitz, C.K. Westbrook, *Combust. Flame* 114 (1998) 149–177.
- [30] S.W. Benson, in: *Thermochemical Kinetics*, Wiley, New York, 1976.
- [31] E.R. Ritter, J.W. Bozzelli, *Int. J. Chem. Kinet.* 23 (1991) 767–778.
- [32] T. Lay, J.W. Bozzelli, A.M. Dean, E.R. Ritter, *J. Phys. Chem.* 99 (1995) 14514–14527.
- [33] R. Sumathi, W.H. Green Jr., *Phys. Chem. Chem. Phys.* 5 (2003) 3402–3417.
- [34] M. O’Conaire, H.J. Curran, J.M. Simmie, W.J. Pitz, C.K. Westbrook, *Int. J. Chem. Kinet.* 36 (2004) 603–622.
- [35] E.L. Petersen, D.M. Kalitan, S. Simmons, G. Bourque, H.J. Curran, J.M. Simmie, *Proc. Combust. Inst.* 31 (2007) 447–454.
- [36] H.J. Curran, P. Gaffuri, W.J. Pitz, C.K. Westbrook, *Combust. Flame* 129 (2002) 253–280.
- [37] C. Sheng, J.W. Bozzelli, A.M. Dean, A.Y. Chang, *J. Phys. Chem. A* 106 (2002) 7276–7293.
- [38] H.J. Curran, *Int. J. Chem. Kinet.* 38 (2006) 250–275.
- [39] P.L. Houston, in: *Chemical Kinetics and Reaction Dynamics*, McGraw–Hill, New York, 2001.
- [40] NIST standard reference database 17 2Q98, 2007, <http://www.nist.gov>.
- [41] A. Rauk, R.J. Boyd, S.L. Boyd, D.J. Henry, L. Radom, *Can. J. Chem.* 81 (2003) 431–442.
- [42] H. Hippler, B. Viskolcz, *Phys. Chem. Chem. Phys.* 4 (2002) 4663–4668.
- [43] J.P. Orme, H.J. Curran, J.M. Simmie, *J. Phys. Chem. A* 110 (2005) 114–131.
- [44] A.T. Blades, H.S. Sandhu, *Int. J. Chem. Kinet.* 3 (1971) 187–193.
- [45] C.M. Lund, L. Chase, Report UCRL-52504, Lawrence Livermore National Laboratory, 1995.
- [46] R.J. Kee, F.M. Rupley, J.A. Miller, M.E. Coltrin, J.F. Grcar, E. Meeks, H.K. Moffat, A.E. Lutz, G. Dixon-Lewis, M.D. Smooke, J. Warnatz, G.H. Evans, R.S. Larson, R.E. Mitchell, L.R. Petzold, W.C. Reynolds, M. Caracotsios, W.E. Steward, P. Glarborg, C. Wang, O. Adigun, Chemkin Collection, Release 3.6, Reaction Design, Inc., San Diego, CA, 2000.
- [47] D.C. Horning, D.F. Davidson, R.K. Hanson, *J. Propuls. Power.* 18 (2002) 363–371.
- [48] J.F. Griffiths, *Prog. Energy Combust. Sci.* 21 (1995) 25–107.

- [49] J. Würmel, E.J. Silke, H.J. Curran, M.S. O’Conaire, J.M. Simmie, *Combust. Flame* 151 (2007) 289–302.
- [50] S.M. Gallagher, H.J. Curran, W.M. Metcalfe, D. Healy, J.M. Simmie, *Combust. Flame*, in press.
- [51] G. Mittal, C.J. Sung, R.A. Yetter, *Int. J. Chem. Kinet.* 38 (2006) 516–529.
- [52] G. Mittal, C.J. Sung, *Combust. Flame* 150 (2007) 355–368.
- [53] E.J. Silke, W.J. Pitz, C.K. Westbrook, M. Ribaucour, J. *Phys. Chem. A* 111 (2007) 3761–3775.
- [54] M. Frenklach, in: W.C. Gardiner Jr. (Ed.), *Combustion Chemistry*, Springer-Verlag, New York, 1984, p. 440.
- [55] C.K. Westbrook, *Proc. Combust. Inst.* 28 (2000) 1563–1577.
- [56] V. Vasudevan, D.F. Davidson, R.K. Hanson, *Int. J. Chem. Kinet.* 37 (2005) 98–109.
- [57] G. Friedrichs, J.T. Herbon, D.F. Davidson, R.K. Hanson, *Phys. Chem. Chem. Phys.* 4 (2002) 5778–5788.
- [58] J. Li, Z. Zhao, A. Kazakov, M. Chaos, F.L. Dryer, J.J. Scire Jr., *Int. J. Chem. Kinet.* 39 (2007) 109–136.
- [59] S. Hochgreb, F.L. Dryer, *Combust. Flame* 91 (1992) 257–284.
- [60] P.A. Glaude, W.J. Pitz, M.J. Thomson, *Proc. Combust. Inst.* 30 (2005) 1111–1118.
- [61] L.R. McCunn, K.C. Lau, M.J. Krisch, L.J. Butler, J.W. Tsung, J.J. Lin, *J. Phys. Chem. A* 110 (2006) 1625–1634.
- [62] J.P. Szybist, J. Song, M. Alam, A.L. Boehman, *Fuel Process. Technol.* 88 (2007) 679–691.
- [63] A. Goldaniga, T. Faravelli, E. Ranzi, P. Dagaut, M. Cathonnet, *Proc. Combust. Inst.* 27 (1998) 353–360.
- [64] J.C. Brocard, F. Baronnet, *Oxid. Commun.* 1 (1980) 321–327.
- [65] A. Ciajola, A. D’Anna, M. Kurz, *Combust. Sci. Technol.* 123 (1997) 49–61.
- [66] C.A. Daly, J.M. Simmie, P. Dagaut, M. Cathonnet, *Combust. Flame* 125 (2001) 1106–1117.
- [67] A. Sinha, M.J. Thomson, *Combust. Flame* 136 (2004) 548–556.